



HAL
open science

Structural and dynamics analysis of intrinsically disordered proteins by high-speed atomic force microscopy

Noriyuki Kodera, Daisuke Noshiro, Sujit K Dora, Tetsuya Mori, Johnny Habchi, David Blocquel, Antoine Gruet, Marion Dosnon, Edoardo Salladini, Christophe Bignon, et al.

► **To cite this version:**

Noriyuki Kodera, Daisuke Noshiro, Sujit K Dora, Tetsuya Mori, Johnny Habchi, et al.. Structural and dynamics analysis of intrinsically disordered proteins by high-speed atomic force microscopy. *Nature Nanotechnology*, 2021, 16 (2), pp.181-189. 10.1038/s41565-020-00798-9 . hal-03362314

HAL Id: hal-03362314

<https://hal.science/hal-03362314>

Submitted on 1 Oct 2021

HAL is a multi-disciplinary open access archive for the deposit and dissemination of scientific research documents, whether they are published or not. The documents may come from teaching and research institutions in France or abroad, or from public or private research centers.

L'archive ouverte pluridisciplinaire **HAL**, est destinée au dépôt et à la diffusion de documents scientifiques de niveau recherche, publiés ou non, émanant des établissements d'enseignement et de recherche français ou étrangers, des laboratoires publics ou privés.

1 **Structural and dynamics analysis of intrinsically disordered proteins by high-**
2 **speed atomic force microscopy**

3 Noriyuki Kodera^{1†}, Daisuke Noshiro^{1†}, Sujit K. Dora^{2†}, Tetsuya Mori², Johnny Habchi³, David Blocquel³,
4 Antoine Gruet³, Marion Dosnon³, Edoardo Salladini³, Christophe Bignon³, Yuko Fujioka⁴, Takashi Oda⁵,
5 Nobuo N. Noda⁴, Mamoru Sato⁵, Marina Lotti⁶, Mineyuki Mizuguchi⁷, Sonia Longhi^{3*} and Toshio
6 Ando^{1*}

7
8 ¹Nano Life Science Institute (WPI-NanoLSI), Kanazawa University, Kakuma-machi, Kanazawa 920-1192,
9 Japan

10 ²Department of Physics, Institute of Science and Engineering, Kanazawa University, Kakuma-machi,
11 Kanazawa 920-1192, Japan

12 ³CNRS and Aix-Marseille Univ, Laboratoire Architecture et Fonction des Macromolécules Biologiques
13 (AFMB), UMR 7257, 13288, Marseille, France

14 ⁴Institute of Microbial Chemistry, Tokyo 141-0021, Japan

15 ⁵Graduate School of Nanobioscience, Yokohama City University, Yokohama 230-0045, Japan

16 ⁶Department of Biotechnology and Biosciences, State University of Milano-Bicocca, Milano, Italy

17 ⁷Faculty of Pharmaceutical Sciences, University of Toyama, 2630 Sugitani, Toyama 930-0194, Japan

18

19 †These authors equally contributed to this work.

20 *Correspondence and requests for materials should be addressed to T.A. (tando@staff.kanazawa-u.ac.jp)
21 or S.L. (sonia.longhi@afmb.univ-mrs.fr).

22

23

24 **Intrinsically disordered proteins (IDPs) are ubiquitous proteins that are disordered entirely**
25 **or partly and play important roles in diverse biological phenomena. Their structure**
26 **dynamically samples a multitude of conformational states, thus rendering their structural**
27 **analysis considerably difficult. Here we explore the potential of high-speed atomic force**
28 **microscopy (HS-AFM) for characterizing the structure and dynamics of IDPs. Successive**
29 **HS-AFM images of an IDP molecule can not only identify constantly folded and constantly**
30 **disordered regions in the molecule but also can document disorder-to-order transitions.**
31 **Moreover, the number of amino acids contained in these disordered regions can roughly be**
32 **estimated, enabling a semi-quantitative, realistic description of the dynamic structure of**
33 **IDPs.**

34

35

36

37 IDPs constitute nearly a half of the entire protein realm^{1,2} and function as hubs in signalling and
38 regulation of transcription, translation and cell cycle³. Our understanding of IDPs however falls
39 far behind that of well-structured proteins. X-ray crystallography and electron microscopy (EM)
40 have no practical application for IDPs because intrinsically disordered regions (IDRs) hamper
41 crystallization and are too thin to be visualized by EM. NMR is so far most instrumental in the
42 structural analysis of IDPs^{4,5} but provides only distance restraints between amino-acid (a.a.)
43 residues separated by < 2 nm. To complement NMR short-range structural information and
44 estimate the overall dimensions of IDPs, small-angle X-ray scattering (SAXS) is used⁶. However,
45 both are ensemble-averaging methods that cannot examine individual conformations and their
46 populations. To mitigate this problem, computational ensemble generation of disordered
47 conformations is attempted by simulations^{7,8} or using statistical distribution of coil conformations
48 from structure databases^{9,10}. Single-molecule Förster resonance energy transfer spectroscopy,
49 which can resolve structural and dynamic heterogeneity, can be used for the structural analysis of
50 chemically denatured proteins and IDPs¹¹⁻¹³. Nevertheless, the donor and acceptor have to be in
51 close proximity ($< \sim 10$ nm). Thus, we still lack versatile techniques enabling simultaneous and
52 temporal assessment of both local (even with semi-residue resolution) and overall structures of
53 IDPs.

54 Here we explored the potential of HS-AFM^{14,15} for structural and dynamics analysis of
55 IDPs. All imaging experiments were performed in amplitude modulation mode, where a
56 cantilever was vertically oscillated at its resonant frequency of ~ 1 MHz in buffer solution. The
57 cantilever free oscillation amplitude and the set point amplitude were set at appropriate values so
58 that the loss of cantilever's oscillation energy *per* tap was adjusted to be $2-3 k_B T$ on average (k_B ,
59 Boltzmann constant; T , room temperature in kelvin) (Supplementary Note 1). This energy, which
60 is considered to be transferred to the specimen, is partitioned into many degrees of freedom in the
61 specimen and dissipates quickly into solution. As demonstrated previously for an IDP, Facilitates
62 Chromatin Transcription (FACT) protein, HS-AFM can visualise the thin and flexible structure
63 of IDRs^{16,17}. These studies, along with numerous previous HS-AFM studies performed on
64 structured proteins^{e.g., 18-21}, have ruled out possible effects of the tip-sample contact on the
65 structural properties and function of the protein under study. The present study on various IDPs
66 shows that HS-AFM can identify at the near residue level the fully disordered regions and the

67 border between disordered and folded regions. Moreover, it provides information on the
68 structural transition dynamics and the structural nature of transiently folded conformations.

69

70 **Structural analysis of PQBP-1 constructs**

71 We first imaged polyglutamine tract binding protein-1 (PQBP-1) and its four deletion
72 constructs with shorter IDRs placed on mica, at 13.1–23.8 frames per second (fps) using HS-
73 AFM (Fig. 1 and Supplementary Table 1). The HS-AFM movie (Supplementary Video 1)
74 revealed that wild type (WT) PQBP-1 has a small globule at one end and a long flexible, thin
75 structure (i.e., IDR) (Fig. 1b, top), consistent with previous NMR data²². The N-terminal segment
76 (1–47), for which no NMR data are available, appeared as being part of the globule containing
77 the ordered WW domain (48–81). In the five constructs (Fig. 1a), the IDRs with average
78 diameter 0.5 ± 0.1 – 0.3 nm (mean \pm standard deviation, s.d.) (Fig. 1e and Supplementary Table 1)
79 appeared constantly disordered. To measure the two-dimensional (2D) end-to-end distance (R_{2D})
80 of the IDRs, the direct distance D between the N-terminal globule and the C-terminal end was
81 measured, followed by measurements of the N-terminal globule height H_1 and the C-terminal end
82 height H_2 . R_{2D} was estimated as $R_{2D} = D - H_1/2 - H_2/2$ (Fig. 1c and Supplementary Note 2).

83 The estimated values of $\langle R_{2D} \rangle$, $\langle H_1 \rangle$ and $\langle H_2 \rangle$ of PQBP-1 (1–214) were independent of
84 the imaging rate within the tested range (6.7–50 fps; Extended Data Fig. 1 and Supplementary
85 Table 2), suggesting no significant structural deformation of the molecule by its contact with the
86 tip. Moreover, in WT PQBP-1 the C-terminus position was circularly distributed around the WW
87 domain (Fig. 2a), and its displacement in the fast scan (X) direction occurring during different
88 time intervals were symmetrically distributed around their zero mean displacement (Fig. 2b). The
89 averaged absolute values of displacements in the X-direction were nearly identical to those in the
90 slow scan (Y) direction (Fig. 2c). Since the HS-FM images were captured during tip scanning
91 relative to the sample stage from $-X$ to $+X$ direction, these data showing no directional bias in
92 the C-terminus displacements ascertain no effect of tip-molecule contact on the IDR motion.
93 Besides, the autocorrelation functions of time series of R_{2D} showed no correlation of its change
94 over time even when the HS-AFM images were captured at 50 fps, suggesting no impediment of
95 the mica surface and tip to IDR diffusional motion in this time scale (Fig. 2d–f).

96 The $\langle R_{2D} \rangle$ values for these constructs were 17.2 ± 0.09 , 14.4 ± 0.14 , 11.0 ± 0.04 , $9.3 \pm$
97 0.07 , and 7.1 ± 0.02 nm (mean \pm standard error, s.e.; Supplementary Note 3) in the order of

98 decreasing construct length (Fig. 1f), approximately following a scaling law $\langle R_{2D} \rangle = \beta_{2D} \times N_{aa}^\nu$
 99 with $\beta_{2D} = 1.18 \pm 0.11$ nm (best fit value \pm s.e.) and $\nu = 0.51 \pm 0.02$. This Flory exponent ν is
 100 close to 0.5, which holds for 2D and three-dimensional (3D) ideal and Gaussian chains²³,
 101 implying that these constantly disordered segments have similar values of persistence length (L_p)
 102 that can be estimated from

$$\langle R_{2D}^2(L) \rangle = 4L_p L \left[1 - \frac{2L_p}{L} \left\{ 1 - \exp\left(-\frac{L}{2L_p}\right) \right\} \right], \quad (1)$$

103 where L represents the contour length of a chain²⁴. For an unstructured polypeptide chain, $L =$
 104 $(N_{aa} - 1) \times \langle d_{aa} \rangle$, where N_{aa} is the number of a.a. contained in the chain and $\langle d_{aa} \rangle$ is the average
 105 distance between two adjacent a.a., with the most likely value of $\langle d_{aa} \rangle$ being 0.36 nm²⁵. The L_p
 106 values estimated for these constructs were 1.16, 1.15, 1.11, 1.35, and 1.45 nm in the order of
 107 decreasing construct length.

108 The chain conformations of these IDRs are very likely to be affected to some extent by
 109 their confinement to the liquid-mica interface because of their significantly flexible nature. To
 110 assess this influence, we performed SAXS measurements in solution (i.e., not on mica) using four
 111 IDRs of PQBP-1 (82–265, 82–214, 82–164 and 82–134), yielding values of radius of gyration
 112 $\langle R_g \rangle$ of 3.62 ± 0.05 , 3.10 ± 0.18 , 2.69 ± 0.04 , and 2.14 ± 0.04 nm, respectively (red circles in Fig.
 113 3n; Extended Data Fig. 2 and Supplementary Table 3). In Gaussian chains, $\langle R_{2D}^2 \rangle$ is
 114 theoretically identical to $2 \times \langle R_{3D}^2 \rangle$, where R_{3D} is the end-to-end distance in solution, and the
 115 value of $\langle R_{3D}^2 \rangle / \langle R_g^2 \rangle$ is 6.0 when $L \gg L_p$ ²⁶. Therefore, we expect $\langle R_{2D}^2 \rangle / \langle R_g^2 \rangle \approx 12.0$.
 116 However, the $\langle R_{2D}^2 \rangle / \langle R_g^2 \rangle$ values of the fully disordered IDRs were significantly larger than
 117 12.0 (20.0 on average), indicating that the mica surface expands the IDR 2D dimensions roughly
 118 by a factor $\sqrt{20/12} \approx 1.3$. Its possible cause could be frictional forces locally exerted from mica
 119 against fast Brownian motion of the IDR chain, which would increase the IDR chain's undulation
 120 wavelength and/or decrease the undulation amplitude, resulting in swelling of its 2D
 121 dimensions²⁷.

122

123 **Structural analysis of autophagy proteins**

124 Next, we imaged autophagy proteins containing longer IDRs, Atg1 (D211A kinase-dead
 125 mutant) and Atg13 (Fig. 3 and Supplementary Videos 2 and 3). The IDR of Atg1 (D211A)
 126 showed a double Gaussian distribution of R_{2D} (Fig. 3h), suggesting interactions between the IDR

127 and the dead kinase domain, in agreement with phosphorylation of the IDR by the N-terminal
128 kinase domain of the WT protein (Extended Data Fig. 3b). The IDR of Atg13 exhibited
129 temporarily appearing and disappearing small globules (Fig. 3d, 9.2 s and 30.0 s), resulting in a
130 double Gaussian distribution of R_{2D} (Fig. 3l). Since the four small regions within the IDR (red
131 bars in Fig. 3c) are known to interact with Atg1 or Atg17²⁸, the small globules probably
132 correspond to these regions. The $\langle R_{2D} \rangle$ values in the longer IDR states of Atg1 and Atg13 were
133 20.5 ± 1.42 and 28.1 ± 4.62 nm (Fig. 3h,l), respectively, and remained nearly unchanged upon pH
134 increase from 6 to 8 for both proteins and upon modification of both salt type and concentration
135 for Atg1 (Fig. 3i,m). In contrast, the $\langle R_{2D} \rangle$ values in the shorter states varied (Extended Data
136 Figs. 3 and 4 and Supplementary Tables 4 and 5). Since the IDRs in the longer states are
137 considered to be fully disordered, we estimated their L_p values using $(N_{aa}, \langle R_{2D} \rangle) = (255, 20.5$
138 $\text{nm})$ for Atg1 and $(N_{aa}, \langle R_{2D} \rangle) = (477, 28.1 \text{ nm})$ for Atg13, yielding L_p of 1.18 and 1.17 nm,
139 respectively. These “measured L_p values” close to each other are also close to those of the IDRs
140 in the PQBP-1 constructs. The height of the C-terminal end of Atg13 was 0.5 ± 0.2 nm (mean \pm
141 s.d.) (Fig. 3k).

142

143 **Structural analysis of N_{TAIL}**

144 Next, we observed the C-terminal domain of the measles virus (MeV) nucleoprotein
145 (N_{TAIL}). Its Box1 (401–420) and Box2 (486–502) regions were previously shown to correspond
146 to a Molecular Recognition Element^{29,30} of helical nature (α -MoRE) in equilibrium among
147 completely unfolded and folded helical conformations^{30–34}. We used N_{TAIL} constructs fused at
148 their N- or C-terminus to GFP or thioredoxin (Trx) to impede the otherwise very fast diffusion of
149 N_{TAIL} . N_{TAIL} -GFP (Fig. 4a) showed a thin and flexible tail-like structure and a C-terminal GFP
150 globule with mean height of 3.2 nm ³⁵ (Fig. 4d,g and Supplementary Video 4). The IDR showed a
151 temporarily appearing and disappearing small globule at the N-terminus corresponding to Box1
152 (Fig. 4d). Except for this, the IDR was observed to be fully disordered (with mean height of
153 $0.4\text{--}0.5 \text{ nm}$) (Extended Data Fig. 5a). Box2 was indiscernible due to its close proximity to GFP
154 but appeared in the images of Trx- N_{TAIL} (Extended Data Fig. 6, Supplementary Fig. 1 and Video
155 5).

156 The R_{2D} histogram of the IDR in N_{TAIL} -GFP showed a single Gaussian peak at 11.6 ± 0.1
157 nm (Fig. 4h and Supplementary Fig. 2), consistent with the very small population of Box1 in the

158 higher state, as observed in both $N_{\text{TAIL}}\text{-GFP}$ (Fig. 4k) and $N_{\text{TAIL}}\text{-Trx}$ (Extended Data Fig. 7f,i and
 159 Supplementary Video 6), and the large population of Box2 in the higher state as observed in Trx-
 160 N_{TAIL} (Extended Data Fig. 6e). From $\langle R_{2D} \rangle = 11.6$ nm and $N_{\text{aa}} = 88$ in the IDRs spanning 421–
 161 485 and 503–525, L_p was estimated to be 1.16 ± 0.02 nm, a value close to those described above.
 162 HS-AFM images of $N_{\text{TAIL}}\text{-Trx}$ also gave similar $\langle R_{2D} \rangle$ values at pH 6.0 and 7.0 (11.2 ± 0.1 and
 163 11.1 ± 0.1 nm, respectively) (Extended Data Fig. 7e,h), yielding L_p values around 1.06 nm.
 164 However, HS-AFM images of $\text{Trx-}N_{\text{TAIL}}$ gave a slightly smaller value, $\langle R_{2D} \rangle = 10.1 \pm 0.1$ nm
 165 (Extended Data Fig. 6d), resulting in a smaller L_p value (0.86 ± 0.02 nm), possibly due to an
 166 increased order propensity of Box1 induced by interaction with the adjacent Trx. To gain more
 167 insights into the structural transitions of Box1 and Box2, we measured their height H_2 . The H_2
 168 histograms of Box1 in $N_{\text{TAIL}}\text{-GFP}$ and $N_{\text{TAIL}}\text{-Trx}$ (at pH 6.0 and 7.0), as well as that of Box2 in
 169 $\text{Trx-}N_{\text{TAIL}}$, showed double Gaussian peaks at 0.8 and 1.1 nm (Fig. 4k, Extended Data Figs. 6e and
 170 7f,i and Supplementary Tables 6 and 7). Moreover, despite the single Gaussian distribution of
 171 R_{2D} , these H_2 distributions were correlated with the corresponding R_{2D} distributions (Fig. 4n and
 172 Supplementary Fig. 3), suggesting that the IDR length partly changes due to order-disorder
 173 transitions in these globules. The order propensity of Box1 and Box2 was estimated from the
 174 population ratios (K_e) between their higher and lower states, yielding $K_e = 0.19\text{--}0.28$ (depending
 175 on the pH value) and $K_e = 1.91$ (at pH 6.0), respectively (Supplementary Tables 6 and 7). The H_2
 176 value of 0.8 nm is larger than the height of fully disordered regions, indicating that Box1 and
 177 Box2 are both partially ordered even in their lower height states. The H_2 value of 1.1 nm is
 178 identical to the diameter of a single α -helix, suggesting that Box1 and Box2 are α -MoREs,
 179 consistent with previous studies^{29,32}. From these features, the dynamic structure of N_{TAIL} could
 180 be sketched (Fig. 4q).

181

182 **Power law for $\langle R_{2D} \rangle$**

183 In the above observations, we used proteins with IDR boundaries previously identified at
 184 the residue level. The $\langle R_{2D} \rangle$ values of these IDRs in their fully disordered state were plotted
 185 against N_{aa} (Fig. 3n), together with a data point ($N_{\text{aa}}, \langle R_{2D} \rangle$) = (121, 14.3 ± 0.18 nm) obtained by
 186 our previous HS-AFM study for a fully disordered IDR in unphosphorylated FACT protein¹⁷.
 187 The nine points could be fitted to a power law $\langle R_{2D} \rangle = \beta_{2D} \times N_{\text{aa}}^v$ with $\beta_{2D} = 1.16 \pm 0.057$ nm and

188 $\nu = 0.52 \pm 0.009$ (blue solid line in Fig. 3n). The mean observed L_p value was 1.18 nm
189 (Supplementary Table 8).

190

191 **Structural analysis of PNT**

192 Although the N-terminal domain of the MeV phosphoprotein (PNT) is mainly disordered,
193 the regions 1–37, 87–93, and 189–198 were shown by NMR to have α -helical propensities, and
194 hence named $\alpha_{1/2}$, α_3 and α_4 , respectively³⁶. α_3 and α_4 are interspaced by an acidic IDR (124–168).
195 The resistance of the N-terminal 27–99 region of PNT to proteolysis in the presence of
196 trifluoroethanol³⁷ (a secondary structure stabilizer^{33,34}), cannot be rationalized from the NMR
197 studies, thus suggesting the existence of a large-scale structure undetectable by NMR. To shed
198 light onto this issue, we imaged a PNT segment (1–229) fused to GFP (PNT-GFP; Fig. 4b). PNT-
199 GFP exhibited a thin and flexible tail-like structure with a temporarily appearing and
200 disappearing small globule at the N-terminal end, together with the C-terminal GFP (Fig. 4e and
201 Supplementary Video 7). In addition, a small globule close to GFP could be occasionally
202 detected (middle panel in Fig. 4e), very likely corresponding to α_4 . The R_{2D} histogram of the IDR
203 was best fitted to a double Gaussian with peaks at 8.9 ± 0.33 and 14.3 ± 9.26 nm (Fig. 4i). The
204 mean height of the IDR was 0.4–0.5 nm, in both metastable shorter and longer states (Extended
205 Data Fig. 5b), indicating that the IDR is fully disordered even upon disorder-to-order transition of
206 the small globule. Unlike R_{2D} , the H_2 histogram of the N-terminal small globule undergoing
207 transitions was best fitted to a single Gaussian with a peak at 1.1 ± 0.003 nm (Fig. 4l). To
208 estimate N_{aa} in the IDR, we used both the power law $\langle R_{2D} \rangle = 1.16 \times N_{aa}^{0.52}$ and $\langle L_p \rangle = 1.18$ nm
209 as obtained above, yielding $N_{aa} = 52$ and $N_{aa} = 129$ from the power law, and $N_{aa} = 54$ and $N_{aa} =$
210 128 from $\langle L_p \rangle$ for the shorter and longer states, respectively. Therefore, the number of a.a.
211 contained in the small globule is roughly estimated to be ~ 175 and ~ 100 for the shorter and
212 longer tail states, respectively (α_4 does not much affect the estimate). The number ~ 100 suggests
213 that $\alpha_{1/2}$, α_3 (87–93) and the IDR segment between them (38–86) are contained in the small
214 globule in both longer and shorter IDR states. Therefore, the region encompassing the N-
215 terminus and helix α_3 always forms a compact structure, explaining the resistance to proteolysis
216 of the N-terminal segment extending to a.a. 99. The number ~ 175 suggests that the structural
217 transitions between the two states mainly occur by association and dissociation between the N-

218 terminal compact structure and the acidic IDR (124–168) (Fig. 4r). Note that $\langle H_2 \rangle = 1.1$ nm
219 possibly corresponds to the height of α -helices contained in the small globule.

220

221 **Structural analysis of Sic1**

222 Finally, using Sic1-GFP (Fig. 4c) we studied this IDP that possesses a propensity to adopt
223 a collapsed chain-like form³⁸. Sic1-GFP exhibited a thin and flexible tail-like structure with a
224 temporarily appearing and disappearing small globule at the N-terminal end, together with the C-
225 terminal GFP (Fig. 4f and Supplementary Video 8). The R_{2D} histogram for the IDR was best
226 fitted to a double Gaussian with peaks at 12.2 ± 0.66 and 20.5 ± 2.14 nm (Fig. 4j). The IDR is
227 fully disordered in both shorter and longer states, as judged from its mean height of 0.4–0.5 nm
228 in both metastable states (Extended Data Fig. 5c,d). The H_2 histogram for the N-terminal small
229 globule undergoing transitions was best fitted to a double Gaussian with peaks at 0.9 ± 0.05 and
230 1.3 ± 0.28 nm (Fig. 4m). The height difference (0.4 nm) between the two states is small,
231 compared to the large difference (8.3 nm) between the two $\langle R_{2D} \rangle$ values, suggesting that the
232 partially folded state has a flattened, collapsed structure, consistent with a previous study³⁸. As
233 done above for PNT-GFP, we estimated N_{aa} contained in the shorter and longer IDRs; we
234 obtained $N_{aa} = 95$ and $N_{aa} = 259$ from the power law and $N_{aa} = 95$ and $N_{aa} = 255$ from $\langle L_P \rangle =$
235 1.18 nm for the shorter and longer states, respectively. Therefore, from the total number of a.a.
236 contained in Sic1 (284), the number of a.a. contained in the small globule was estimated to be
237 ~ 30 and ~ 190 for its lower and higher states, respectively. The large number ~ 190 indicates that
238 as much as $\sim 65\%$ of the whole protein is loosely folded, with only the remaining C-terminal
239 region (encompassing roughly 95 a.a) being fully extended. The remarkable difference between
240 ~ 30 and ~ 190 indicates that a large segment containing ~ 160 residues undergoes a transition
241 between fully unstructured and loosely folded conformations (Fig. 4s). The folding propensity
242 derived from the H_2 distribution ($K_e = 1.6$) is close to that estimated from the R_{2D} distribution (K_e
243 $= 1.5$).

244

245 **Order propensity and structural transition dynamics**

246 From all K_e values obtained above, we can infer, for all small globules undergoing
247 transitions, the following relative order propensity: PNT > Box2 (N_{TAIL}) > Sic1 \gg Box1 (N_{TAIL})
248 (Fig. 4q–s and Supplementary Tables 6 and 7). Disorder predictions failed to detect these subtle

249 differences (Supplementary Figs. 4 and 5), underlining the importance of experimental analysis
250 of order-disorder transitions. The order propensity and the transiently ordered structures very
251 likely dictate key features in binding of these IDPs to their targets (Supplementary Note 4). Next,
252 we calculated auto-correlation functions $G(\tau)$ s for time-series $H_2(t)$ or $R_{2D}(t)$ data of these IDPs to
253 estimate the order-to-disorder and disorder-to-order transition rates (k_{OD} and k_{DO} , respectively).
254 The rate constants can be expressed as $k_{OD} = \lambda/(1 + K_e)$ and $k_{DO} = \lambda K_e/(1 + K_e)$, where $\lambda \equiv k_{OD} +$
255 k_{DO} is the decay rate of $G(\tau)$. All $G(\tau)$ s were best fitted to single exponential functions (Fig.
256 2g–m). Time correlations in the $G(\tau)$ s for $R_{2D}(t)$ (Fig. 2k,m) reflect the order/disorder transitions,
257 because Brownian undulation motion of constantly disordered IDRs in PQBP-1 constructs is too
258 fast to appear in $G(\tau)$ (Fig. 2d–f). In fact, in Sic1 the $G(\tau)$ s for $H_2(t)$ and $R_{2D}(t)$ were nearly
259 identical (Fig. 2l,m). In contrast to the widely varying lifetime of the ordered state (0.16–1.89 s)
260 among these IDPs, the lifetime of disordered state does not vary much (0.49–0.94 s) (see Fig.
261 4q–s and Supplementary Table 6).

262

263 **Refinement of mica effect, power law and L_p**

264 SAXS data of non-canonical IDPs obtained by truncation of foldable proteins yielded $\nu =$
265 0.54, despite their hydrophobic nature³⁹. SAXS data of chemically denatured proteins yielded $\nu =$
266 0.598⁴⁰, indicating that chemically denatured proteins are more extended than native IDRs^{11,41}
267 and behave as polymer chains in good solvent (theoretically $\nu = 0.6^{23}$ or 0.588^{42}). In contrast,
268 $\langle R_g \rangle$ vs. N_{aa} plots for 72 naturally occurring IDPs without permanent secondary structures were
269 found to be largely scattered⁴³, possibly due to residual structure leading to varied compactness.
270 In fact, this inference is corroborated by detailed structural analyses for some of the 72 IDPs^{44–48}
271 (Supplementary Note 5). Here we should emphasize that unlike SAXS, our HS-AFM method can
272 single out IDRs in the fully disordered state even when they undergo disorder-order transitions.
273 We here selected ten tau-protein constructs that are not significantly affected by the extended
274 repeat domains and phosphor-mimic mutation⁴⁷. Then, we combined those $\langle R_g \rangle$ data with those
275 of the four PQBP-1 constructs herein reported. Fitting this data set to a power law yielded $\langle R_g \rangle =$
276 $(0.25 \pm 0.038) \times N_{aa}^{0.53 \pm 0.028}$ (Supplementary Fig. 6). A very close power law ($\langle R_g \rangle = 0.254 \times$
277 $N_{aa}^{0.522}$) was previously obtained for several IDRs from their theoretical $\langle R_g \rangle$ values calculated
278 using the coil database⁴⁹. This agreement prompted us to use these 14 experimental (N_{aa} , $\langle R_g \rangle$)
279 data to quantitate more accurately the expansion effect of the mica surface on $\langle R_{2D} \rangle$, while

280 assuming that this effect is independent of N_{aa} . The measured $\langle R_{2D} \rangle$ values of the IDRs (in the
281 longer state when undergoing transitions) were converted to corresponding $\langle R_g \rangle$ values as $\langle R_g \rangle$
282 $= \langle R_{2D} \rangle / (2\sqrt{3}u)$, where u is the expansion factor. Then, these nine (N_{aa} , $\langle R_g \rangle$) data containing the
283 parameter u were combined with the above fourteen SAXS data of (N_{aa} , $\langle R_g \rangle$). Finally, the
284 combined data were fitted to a power law, yielding $u = 1.24 \pm 0.01$ and a fitted curve of $\langle R_g \rangle =$
285 $(0.26 \pm 0.02) \times N_{aa}^{0.52 \pm 0.015}$, from which all data points only slightly deviated (Extended Data Fig.
286 8a). From the $\langle R_g(u) \rangle$ values at $u = 1.24$ for the nine IDRs, their L_p values in solution were
287 calculated (Supplementary Table 8), yielding $\langle L_p \rangle = 0.78 \pm 0.06$ nm. Similar L_p values can be
288 found in various IDPs^{12,13,43} (Extended Data Fig. 8b and Supplementary Table 9).

289 Despite the rather small deviations of data points from the power laws of $\langle R_g \rangle = 0.26 \times$
290 $N_{aa}^{0.52}$ and $\langle R_{2D} \rangle = 1.16 \times N_{aa}^{0.52}$, it is advised to avoid generalization of these power laws or the
291 mean L_p values of 0.78 nm in solution and 1.18 nm on mica to all naturally occurring IDRs in
292 their fully disordered state. Indeed, they cannot be applied to IDRs with a high charge density, a
293 large fraction of charged residues (FCR) or largely segregated oppositely charged residues
294 characterized by large values of κ (see Supplementary Note 6 and Extended Data Fig. 9). The
295 global structure of IDRs has been indeed shown to be modulated by electrostatic effects, i.e. a
296 high charge density swells the volume of an IDR^{11,50}, whereas a combination of large FCR and
297 large κ values results in protein compaction^{51,52}. All IDPs randomly chosen in this study do not
298 possess high charge densities or large values of FCR and κ (Supplementary Table 10); their
299 charge densities (ρ) range between -0.087 and $+0.038$. Small charge densities $|\rho| \leq 0.1$ are often
300 seen in numerous naturally occurring IDRs (50.9% of all IDRs deposited in the Database of
301 Protein Disorder; Extended Data Fig. 9). Although the a.a. sequence and composition of an IDR
302 modulate its conformational sampling at various extents, we resorted to use the power law and
303 the mean L_p value on mica to make a rough estimate of the number of a.a. (N_{aa}) encompassed by
304 the fully disordered IDRs contained in PNT and Sic1. The delineation from this N_{aa} estimation of
305 the global structure of PNT and its transitions appear to be consistent with the domain diagram
306 given by the recent NMR analysis of PNT³⁶ and with its proteolytic pattern³⁷. In the case of Sic1,
307 the reliability of our quantitative estimation of its global structure and transitions cannot be
308 assessed because structural information is currently limited. With the above-mentioned caveats,
309 the power laws and mean L_p values on mica and in solution obtained above appear to be useful

310 for semi-quantitative delineation of the structure and dynamics of IDPs, especially taking into
311 account the current paucity of more useful means for this analysis.

312

313 **Conclusion**

314 HS-AFM imaging of IDPs on mica can distinguish fully and partially disordered regions
315 as well as fully ordered regions at the near residue level, without fragmentation of the entire chain
316 into shorter pieces. Moreover, HS-AFM imaging can provide not only length and height
317 distributions for distinct regions in an IDP but also information on the structural nature of the
318 transiently folded structures (e.g., α -helix and flattened, collapsed structure) and their order
319 propensity and transition dynamics. Thus, HS-AFM imaging is an extremely powerful technique
320 for characterizing IDPs, in particular allowing resolving conformational heterogeneity and
321 avoiding the complications arising from ensemble averaging. Thus, when all molecular features
322 revealed by HS-AFM are combined with the folded local structure given by NMR, the combined
323 information allows a quantitative delineation of the structural and dynamic characters of IDPs, in
324 a more realistic manner compared to the pictures depicted individually, as demonstrated for PNT.

325

326 **Methods**

327 Methods and any associated references are available in the online version of the paper.

328

329 **Data availability**

330 All data that support the findings of this study have been included in the main text, Extended
331 Data Figures and Supplementary Information. The original source data associated with all figures
332 are attached to respective figures.

333 **Code availability**

334 The original code for AFM image analyses is opened to the public at the following web site:

335 <https://elifesciences.org/content/4/e04806/article-data#fig-data-supplementary-material>

336

337 **Additional information**

338 Supplementary information and videos are available in the online version of the paper. Reprints
339 and permission information is available online at www.nature.com/reprints. Correspondence and
340 requests for materials should be addressed to T. Ando or S. Longhi.

341

342 **REFERENCES**

- 343 1. Romero, P. et al. Thousands of proteins likely to have long disordered regions. *Pac. Symp.*
344 *Biocomp.* 3, 437–448 (1998).
- 345 2. Uversky, V. N., Gillespie, J. R. & Fink A. L. Why are “natively unfolded” proteins
346 unstructured under physiologic conditions? *Proteins* 41, 415–427 (2000).
- 347 3. Wright, P. E. & Dyson, H. J. Intrinsically disordered proteins in cellular signaling and
348 regulation. *Nat. Rev. Mol. Cell Biol.* 16, 18–29 (2015).
- 349 4. Dyson, H. J. & Wright, P. E. Unfolded proteins and protein folding studied by NMR. *Chem.*
350 *Rev.* 104, 3607–3622 (2004).
- 351 5. Jensen, M. R., Zweckstetter, M., Huang, J. & Blackledge, M. Exploring free-energy
352 landscapes of intrinsically disordered proteins at atomic resolution using NMR spectroscopy.
353 *Chem. Rev.* 114, 6632–6660 (2014).
- 354 6. Kikhney, A. G. & Svergun, D. I. A practical guide to small angle X-ray scattering (SAXS) of
355 flexible and intrinsically disordered proteins. *FEBS Lett.* 589, 2570–2577 (2015).
- 356 7. Dedmon M., Lindorff-Larsen, K., Christodoulou, J., Vendruscolo, M., Dobson, C. M.
357 Mapping long-range interactions in alphasynuclein using spin-label NMR and ensemble
358 molecular dynamics simulations. *J. Am. Chem. Soc.* 127, 476–477 (2005).
- 359 8. Henriques, J., Cragnell, C. & Skepö, M. Molecular dynamics simulations of intrinsically
360 disordered proteins: force field evaluation and comparison with experiment. *J. Chem. Theory.*
361 *Comput.* 11, 3420-3431 (2015).
- 362 9. Bernadó, P. et al. A structural model for unfolded proteins from residual dipolar couplings
363 and small-angle x-ray scattering. *Proc. Natl. Acad. Sci. U. S. A.* 102,17002–17007 (2005).
- 364 10. Ozenne, V. et al. Flexible-meccano: A tool for the generation of explicit ensemble
365 descriptions of intrinsically disordered proteins and their associated experimental observables.
366 *Bioinformatics* 28,1463-1470 (2012).

- 367 11. Schuler, B., Soranno, A., Hofmann, H. & Nettels, D. Single-molecule FRET spectroscopy
368 and the polymer physics of unfolded and intrinsically disordered proteins. *Annu. Rev.*
369 *Biophys.* 45, 207–231 (2016).
- 370 12. Borgia, A., et al. Consistent view of polypeptide chain expansion in chemical denaturants
371 from multiple experimental methods. *J. Am. Chem. Soc.* 138, 11714–11726 (2016).
- 372 13. Fuertes, G. et al. Decoupling of size and shape fluctuations in heteropolymeric sequences
373 reconciles discrepancies in SAXS vs. FRET measurements. *Proc. Natl. Acad. Sci. U. S. A.*
374 114, E6342–E6351 (2017).
- 375 14. Ando, T. et al. A High-speed atomic force microscope for studying biological
376 macromolecules. *Proc. Natl. Acad. Sci. U. S. A.* 98, 12468–12472 (2001).
- 377 15. Ando, T., Uchihashi, T. & Fukuma, T. High-speed atomic force microscopy for nano-
378 visualization of dynamic biomolecular processes. *Prog. Surf. Sci.* 83, 337–437 (2008).
- 379 16. Miyagi, A. et al. Visualization of intrinsically disordered regions of proteins by high-speed
380 atomic force microscopy, *Chem. Phys. Chem.* 9, 1859–1866 (2008).
- 381 17. Hashimoto, M. et al. Phosphorylation-coupled intramolecular dynamics of unstructured
382 regions in chromatin remodeler FACT. *Biophys. J.* 104, 2222–2234 (2013).
- 383 18. Uchihashi, T., Iino, R., Ando, T. & Noji, H. High-speed atomic force microscopy reveals
384 rotary catalysis of rotorless F_1 -ATPase. *Science* 333, 755–758 (2011).
- 385 19. Kodera, N., Yamamoto, T., Ishikawa, R. & Ando, T. Video imaging of walking myosin V by
386 high-speed atomic force microscopy. *Nature* 468, 72–76 (2010).
- 387 20. Ando, T., Uchihashi, T. & Scheuring, S. Filming biomolecular processes by high-speed
388 atomic force microscopy. *Chem. Rev.* 114, 3120–3188 (2014).
- 389 21. Ando, T. High-speed atomic force microscopy. *Curr. Opin. Chem. Biol.* 51, 105–112 (2019).
- 390 22. Takahashi, M. et al. Polyglutamine tract binding protein-1 is an intrinsically unstructured
391 protein. *Biochim. Biophys. Acta* 1794, 936–943 (2009).

- 392 23. de Gennes, P. –G. Scaling concepts in polymer physics. Cornell University Press, Ithaca and
393 London (1979).
- 394 24. Frontali, C. Excluded-volume effect on the bidimensional conformation of DNA molecules
395 adsorbed to protein films. *Biopolymers* 27, 1329–1331 (1988).
- 396 25. Pérez, J., Vachette, P., Russo, D., Desmadril, M. & Durand, D. Heat-induced unfolding of
397 neocarzinostatin, a small all-beta protein investigated by small-angle X-ray scattering. *J. Mol.*
398 *Biol.* 308, 721–743 (2001).
- 399 26. Iwao, T. *Polymer Solutions: An Introduction to Physical Properties*, John Wiley & Sons, Inc.,
400 New York (2002).
- 401 27. Kirk, J. & Ilg, P. Chain dynamics in polymer melts at flat surfaces. *Macromolecules* 50,
402 3703–3718 (2017).
- 403 28. Yamamoto, H. et al. The intrinsically disordered protein Atg13 mediates supramolecular
404 assembly of autophagy initiation complexes. *Dev. Cell* 38, 86–99 (2016).
- 405 29. Mohan, A. et al. Analysis of molecular recognition features (MoRFs). *J. Mol. Biol.* 362,
406 1043–1059 (2006).
- 407 30. Jensen, M. R. et al. Intrinsic disorder in measles virus nucleocapsids. *Proc. Natl. Acad. Sci. U.*
408 *S. A.* 108, 9839–9844 (2011).
- 409 31. Gely, S. et al. Solution structure of the C-terminal X domain of the measles virus
410 phosphoprotein and interaction with the intrinsically disordered C-terminal domain of the
411 nucleoprotein. *J. Mol. Recognit.* 23, 435–447 (2010).
- 412 32. Oldfield, C. J. et al. Coupled folding and binding with α -helix-forming molecular recognition
413 elements. *Biochemistry* 44, 12454–12470 (2005).
- 414 33. Morin, B. et al. Assessing induced folding of an intrinsically disordered protein by site-
415 directed spin-labeling electron paramagnetic resonance spectroscopy. *J. Phys. Chem. B* 110,
416 20596–20608 (2006).

- 417 34. Belle, V. et al. Mapping α -helical induced folding within the intrinsically disordered C-
418 terminal domain of the measles virus nucleoprotein by site-directed spin-labeling EPR
419 spectroscopy. *Proteins* 73, 973–988 (2008).
- 420 35. Ormö, M., Cubitt, A. B., Kallio, K., Gross, L. A., Tsien, R. Y. & Remington, S. J. Crystal
421 structure of the *Aequorea victoria* green fluorescent protein. *Science* 273, 1392–1395 (1996).
- 422 36. Milles, S. et al. An ultraweak interaction in the intrinsically disordered replication machinery
423 is essential for measles virus function. *Sci. Adv.* 4, eaat7778 (2018).
- 424 37. Habchi, J., Mamelli, L., Darbon, H. & Longhi, S. Structural disorder within henipavirus
425 nucleoprotein and phosphoprotein: From predictions to experimental assessment. *PLoS One* 5,
426 e11684 (2010).
- 427 38. Brocca, S. et al. Compaction properties of an intrinsically disordered protein: Sic1 and its
428 kinase-inhibitor domain. *Biophys. J.* 100, 2243–2252 (2011).
- 429 39. Riback, J. A. et al. Innovative scattering analysis shows that hydrophobic disordered proteins
430 are expanded in water. *Science* 358, 238–241 (2017).
- 431 40. Kohn, J. E. et al. Random-coil behavior and the dimensions of chemically unfolded proteins.
432 *Proc. Natl. Acad. Sci. U. S. A.* 101, 12491–12496 (2004).
- 433 41. Meier, S., Grzesiek, S. & Blackledge, M. Mapping the conformational landscape of urea-
434 denatured ubiquitin using residual dipolar couplings. *J. Am. Chem. Soc.* 129, 9799–9807
435 (2007).
- 436 42. Le Guillo, J. C. & Zinn-Justin, J. Critical exponents for the n-vector model in three
437 dimensions from field theory. *Phys. Rev. Lett.* 39, 95–98 (1977).
- 438 43. Cordeiro, T. N. et al. Structural characterization of highly flexible proteins by small-angle
439 scattering. *Adv. Exp. Med. Biol.* 1009, 107–129 (2017).
- 440 44. Boze, H. et al. Proline-rich salivary proteins have extended conformations. *Biophys. J.* 99,
441 656–665 (2010).

- 442 45. Kate M. Nairn, K. M. et al. A synthetic resilin is largely unstructured. *Biophys. J.* 95, 3358–
443 3365 (2008).
- 444 46. Salmon, L. et al. NMR characterization of long-range order in intrinsically disordered
445 proteins. *J. Am. Chem. Soc.* 132, 8407–8418 (2010).
- 446 47. Mylonas, E. et al. Domain conformation of tau protein studied by solution small-angle X-ray
447 scattering. *Biochemistry* 47, 10345–10353 (2008).
- 448 48. Lanza, D. C., Silva, J. C., Assmann, E. M., Quaresma, A. J., Bressan, G. C., Torriani, I. L. &
449 Kobarg, J. Human FEZ1 has characteristics of a natively unfolded protein and dimerizes in
450 solution. *Proteins* 74, 104–21 (2009).
- 451 49. Bernadó, P. & Blackledge, M. A. Self-consistent description of the conformational behavior
452 of chemically denatured proteins from NMR and small angle scattering. *Biophys. J.* 97, 2839–
453 2845 (2009).
- 454 50. Müller-Späth, S. et al. Charge interactions can dominate the dimensions of intrinsically
455 disordered proteins. *Proc. Natl. Acad. U. S. A.* 107, 14609–14614 (2010).
- 456 51. Das, R. K., Huang, Y., Phillips, A. H., Kriwacki, R. W. & Pappu, R. V. Cryptic sequence
457 features within the disordered protein p27Kip1 regulate cell cycle signalling. *Proc. Natl. Acad.*
458 *Sci. U. S. A.* 113, 5616–5621 (2016).
- 459 52. Sherrya, K. P., Das, R. K., Pappu, R. V. & Barricka, D. Control of transcriptional activity by
460 design of charge patterning in the intrinsically disordered RAM region of the Notch receptor.
461 *Proc. Natl. Acad. Sci. U. S. A.* 114, E9243–E9252 (2017).

462

463 **ACKNOWLEDGMENTS**

464 We thank Ms. Maya Hakozaki (Kanazawa University) for her technical assistance, Dr. Hitoshi
465 Okazawa (Tokyo Medical and Dental University) for providing the human PQBP-1 cDNA, and
466 Antoine Schramn (Lab. AFMB UMR 7257, Aix-Marseille University and CNRS) for providing
467 the statistics of IDRs deposited in the DisProt database. This work was supported by grants from
468 the MEXT, Japan, Grants-in-Aid for Scientific Research on Innovative Areas: Research in a

469 Proposed Research Area, #21113002 and #26119003 (T.A.), #21113003 (M.M.), #15H01651
470 (Y.F.) and #25111004 (N.N.N.), Grant-in-Aid for Basic Research S, #24227005 and #17H06121
471 (T.A.), CREST program of JST (T.A. and N.N.N.) and PRESTO program of JST (N.K.), and
472 partly supported by grants from the Agence Nationale de la Recherche, specific programs
473 ‘Microbiologie et Immunologie’ ANR-05-MIIM-035-02 (S.L.) and ‘Physico-Chimie du Vivant’
474 ANR-08-PCVI-0020-01 (S.L.). D.B. was supported by a joint doctoral fellowship from the
475 Direction Générale de l’Armement (DGA) and the CNRS. E.S. was supported by a joint doctoral
476 fellowship from the Direction Générale de l’Armement (DGA) and Aix-Marseille Université.
477 M.D. was supported by a PhD fellowship from the French Ministry of National Education,
478 Research and Technology.

479

480 **AUTHOR CONTRIBUTIONS**

481 S.L. and T.A. designed the project. M.L. provided the original constructs encoding GFP fusions.
482 M.M, D.B., J.H., A.G, M.D., E.S., C.B., Y.F. and N.N.N. prepared constructs and/or protein
483 samples used in this study. T.A. and N.K. developed the HS-AFM system. N.K., D.N., S.K.D.
484 and T.M. performed the HS-AFM experiments. N.K., T.A., D.N., S.K.D. and T.M. analyzed HS-
485 AFM data. T.O. and M.S. performed the SAXS experiments and analyzed SAXS data. T.A. made
486 all theoretical formulations and wrote the draft of the manuscript. S.L., N.K. and T.A. prepared
487 the final manuscript based on the discussions performed among all authors.

488

489 **Competing interests**

490 There is no financial competing interest.

491

492

493

494

495

496

497

498

499

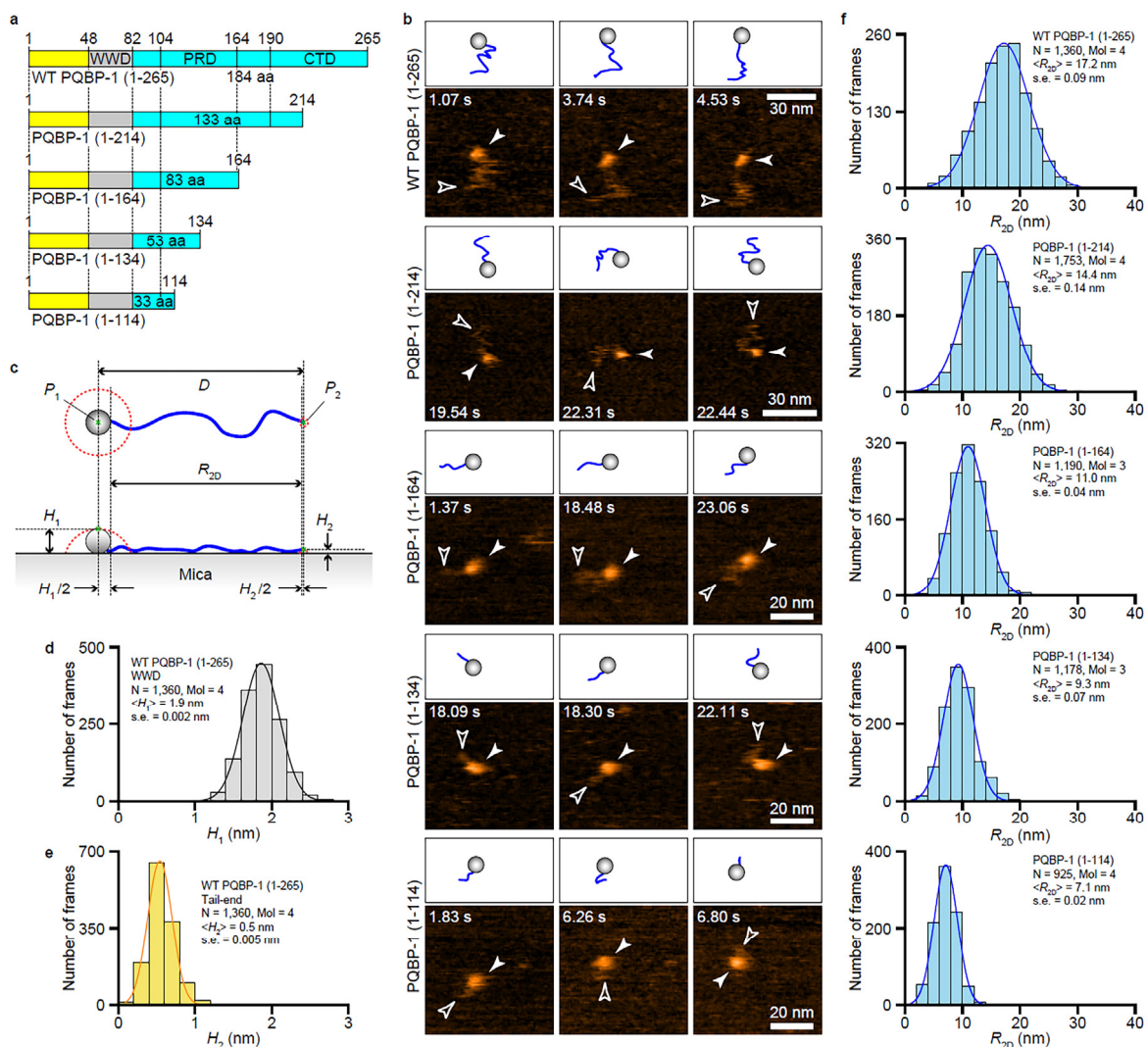
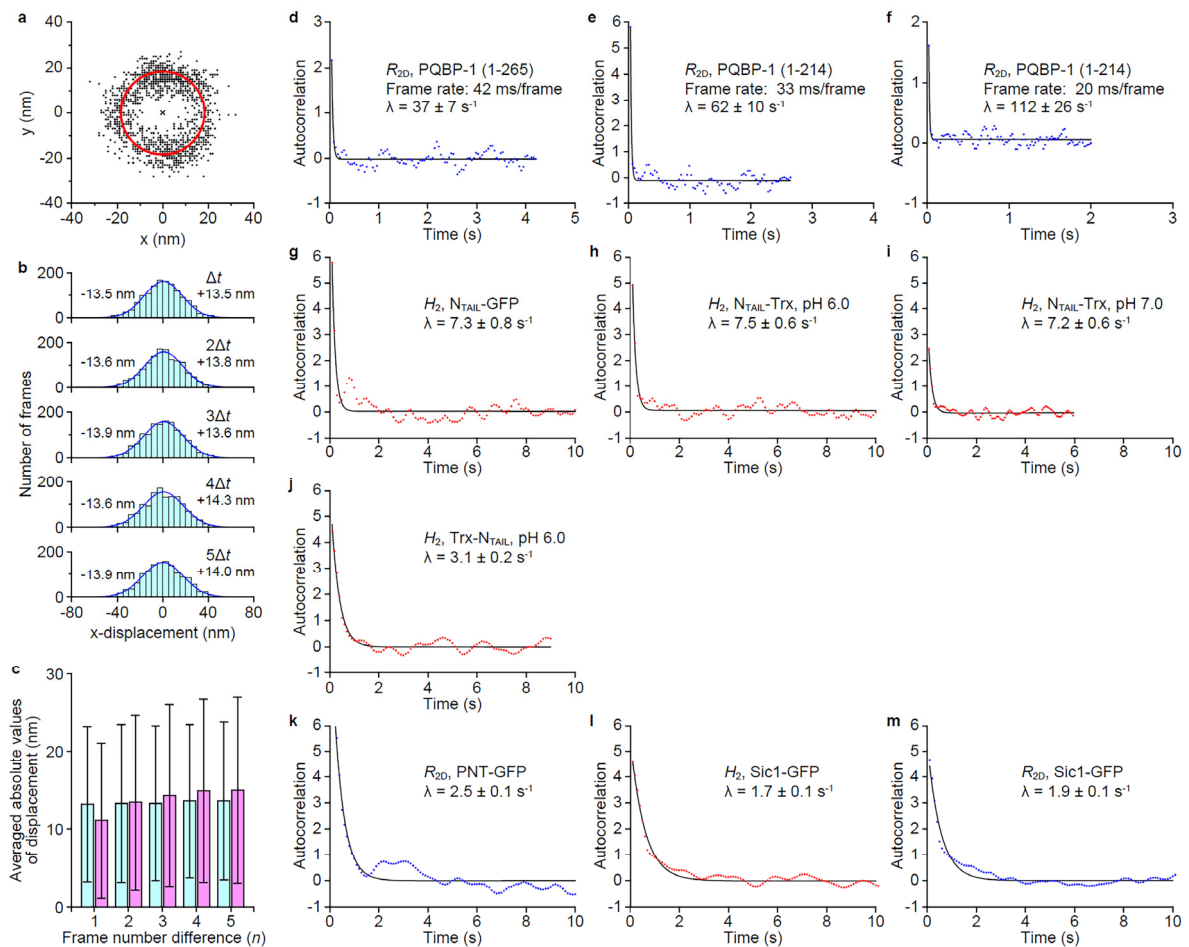


Figure 1 | Structural features of PQBP-1 constructs revealed by HS-AFM imaging. **a**, Domain diagrams of five PQBP-1 constructs containing IDRs (light blue), folded WWD (gray) and the N-terminal segment not investigated with NMR (yellow). **b**, HS-AFM images and schematized molecular features of PQBP-1 constructs. Z-scale, 0.0–3.5 nm. **c**, Schematics showing the observed molecular characteristics of the PQBP-1 constructs (Top, top-view; Bottom, side-view): Gray spheres, N-terminal globular domain; blue thick solid lines, IDRs; dashed red lines, schematic topographies of the globular domain convoluted with the finite size of the tip apex in lateral contact with the globule. **d,e**, Height distributions of globule (**d**) and tail end (**e**) in WT PQBP-1. **f**, R_{2D} distributions of tail-like segments in PQBP-1 constructs. Solid blue lines show most probable fitting curves. The values obtained by Gaussian distribution fitting are mean \pm standard error (s.e.). This definition is the same for all Gaussian fitting results in this paper, unless otherwise stated. “Mol” in (**d–f**) indicates the number of molecules analysed. This is the same for **Figs. 3** and **4**.



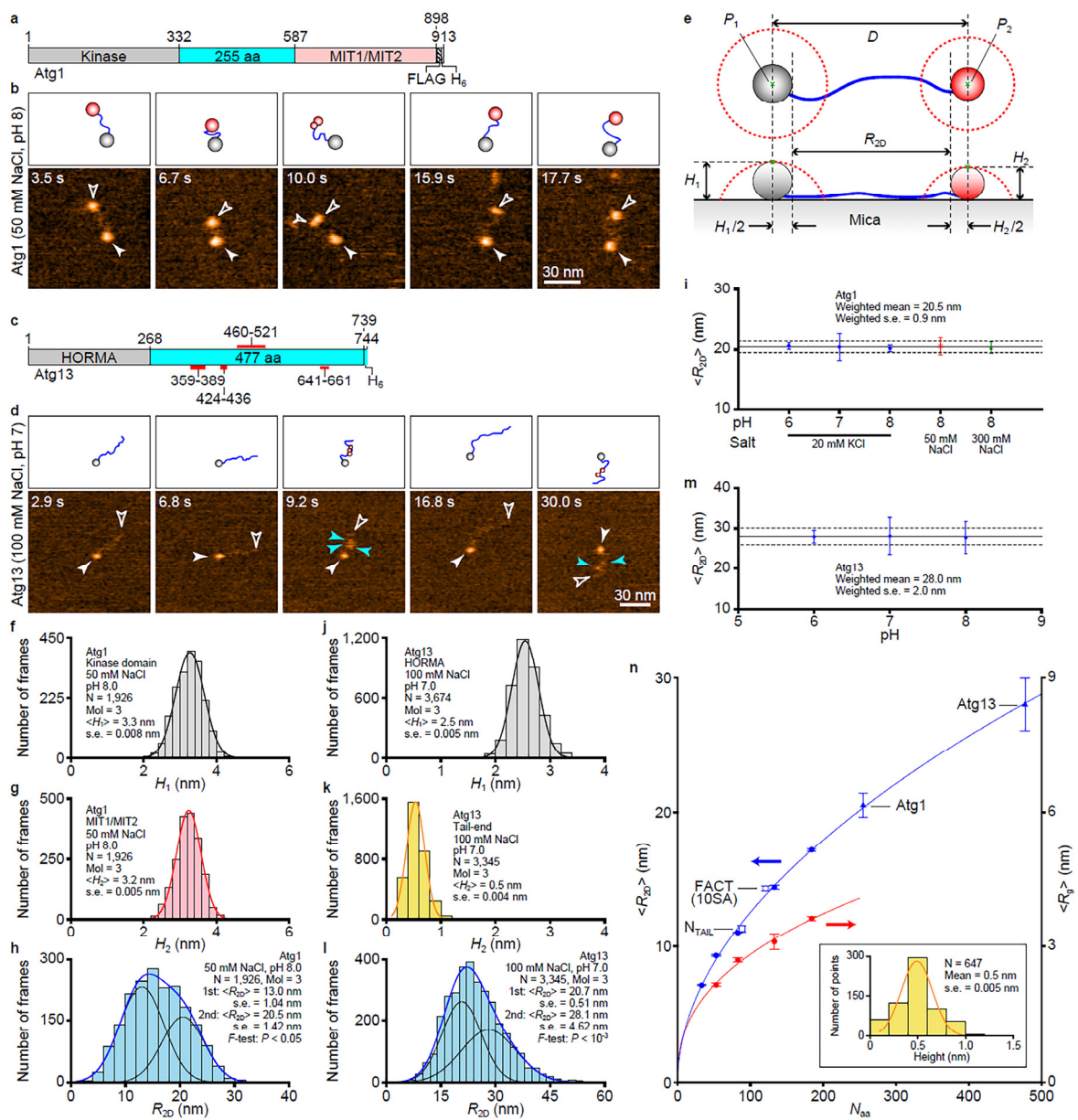


Figure 3 | Structural features of Atg1 and Atg13 revealed by HS-AFM imaging and $\langle R_{2D} \rangle - N_{aa}$ and $\langle R_g \rangle - N_{aa}$ relationships. **a,c**, Domain diagrams of Atg1 (D211A) (**a**) and Atg13 (**c**); the top and bottom red bars in **c** are Atg1- and Atg17-binding regions, respectively. **b,d**, HS-AFM images and their schematics of Atg1 (D211A) (**b**) and Atg13 (**d**). Z-scale, 0.0–3.5 nm. Light-blue arrow-heads (**d**, 9.2 s and 30.0 s) indicate temporarily appearing small globules. **e**, Schematics of observed molecular features of Atg1 (D211A) (Top, top-view; Bottom, side-view). **f,g,j,k**, Height distributions of kinase (**f**), MIT1/MIT2 (**g**) and HORMA (**j**) domains and C-terminal end of Atg13 (**k**). **h,i**, R_{2D} distributions of Atg1 (D211A) (**h**) and Atg13 (**i**). **i**, Dependence of $\langle R_{2D} \rangle$ in the longer state of Atg1 (D211A) on pH and salt type and concentration. **m**, pH dependence of $\langle R_{2D} \rangle$ in the longer state of Atg13. **n**, $\langle R_{2D} \rangle - N_{aa}$ relationship (blue line) from $\langle R_{2D} \rangle$ data of PQBP-1 (closed blue circles), FACT (IDR in the SSRP1 subunit)²¹, N_{TAIL} , Atg1 (D211A) and Atg13, and $\langle R_g \rangle - N_{aa}$ relationship from SAXS data of IDRs in PQBP-1 (closed red circles). The $\langle R_{2D} \rangle$ values for the Atg proteins are those in the longer states. Inset: height distribution of constantly disordered IDR in WT PQBP-1.

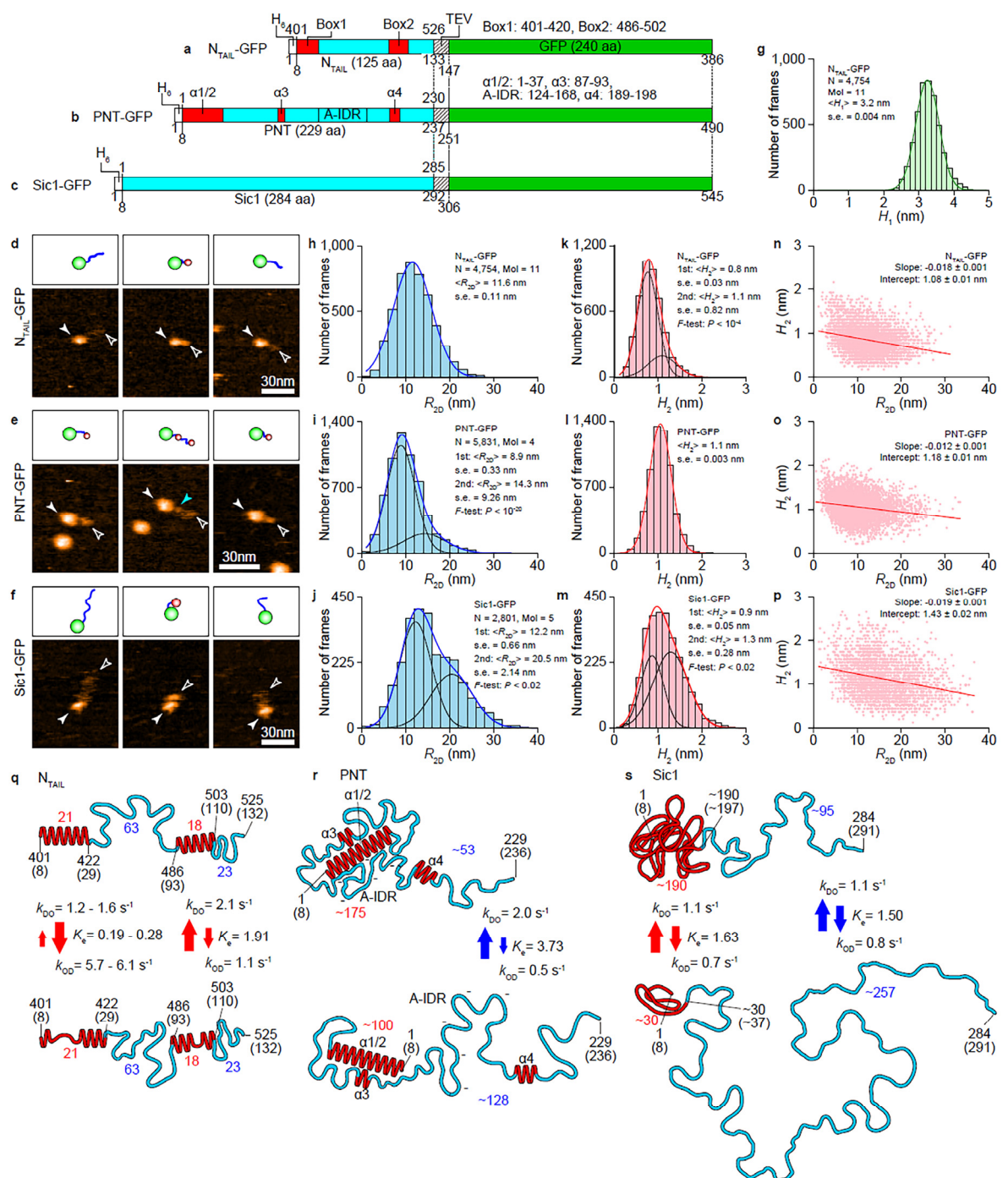
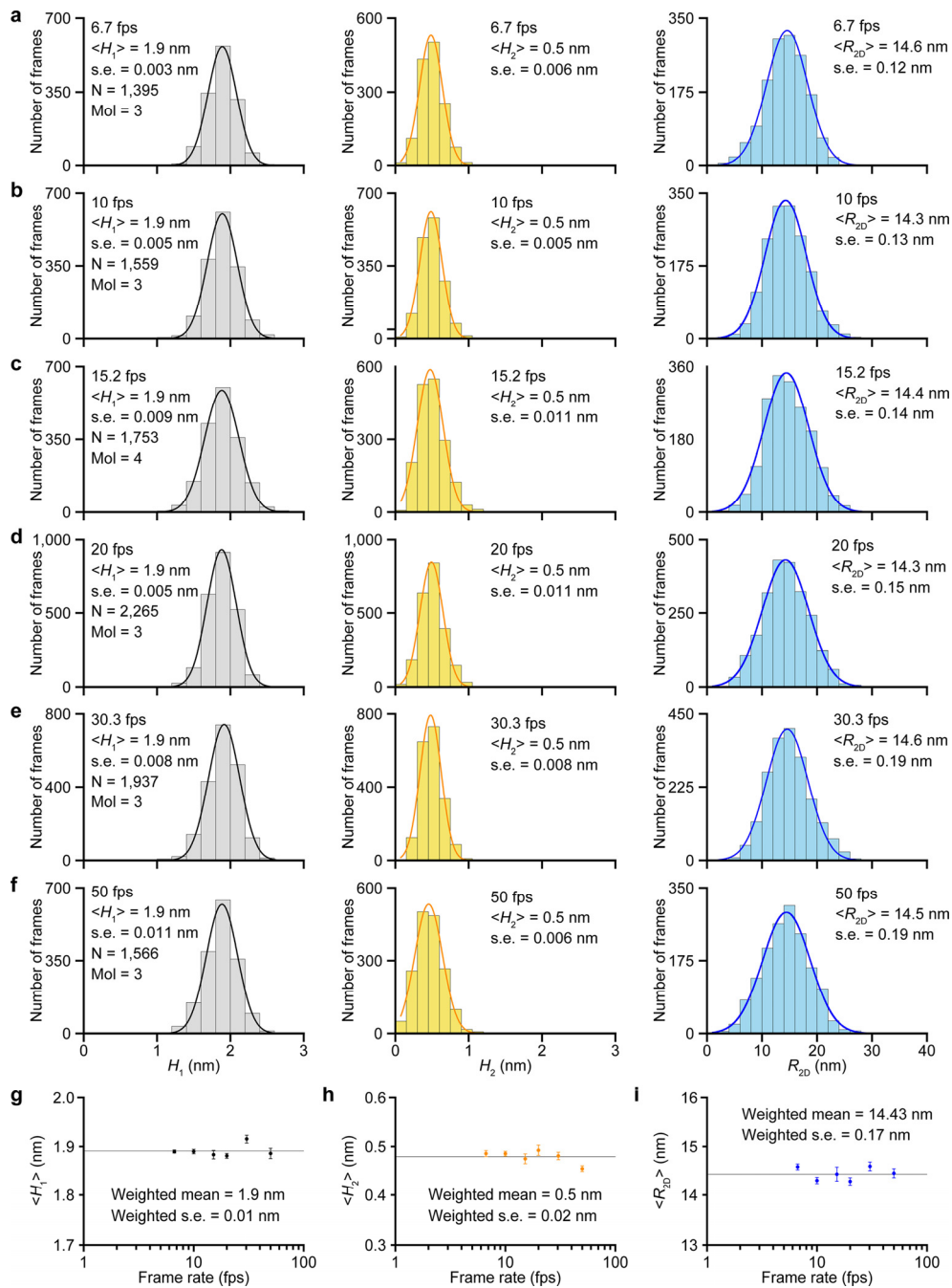
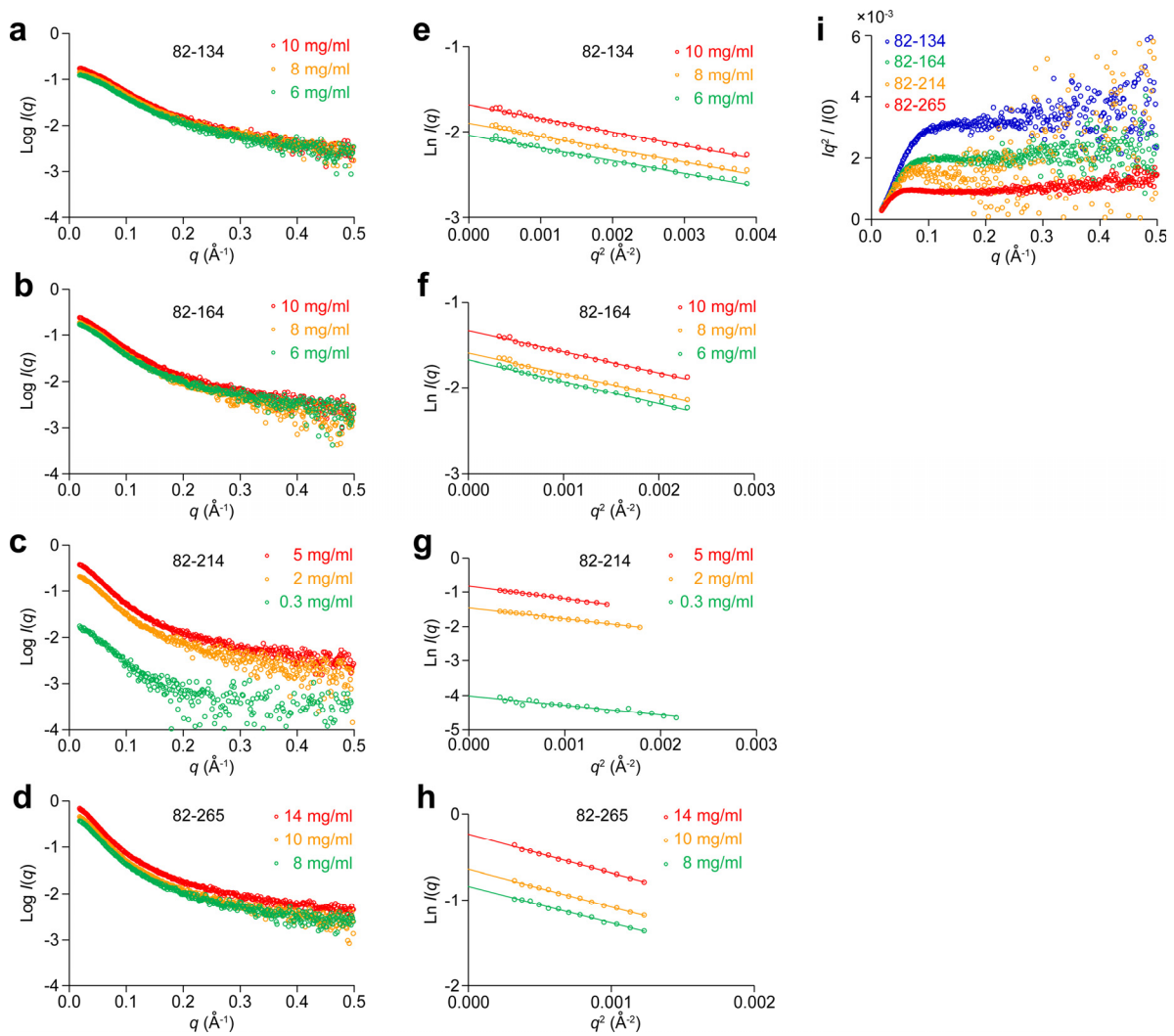


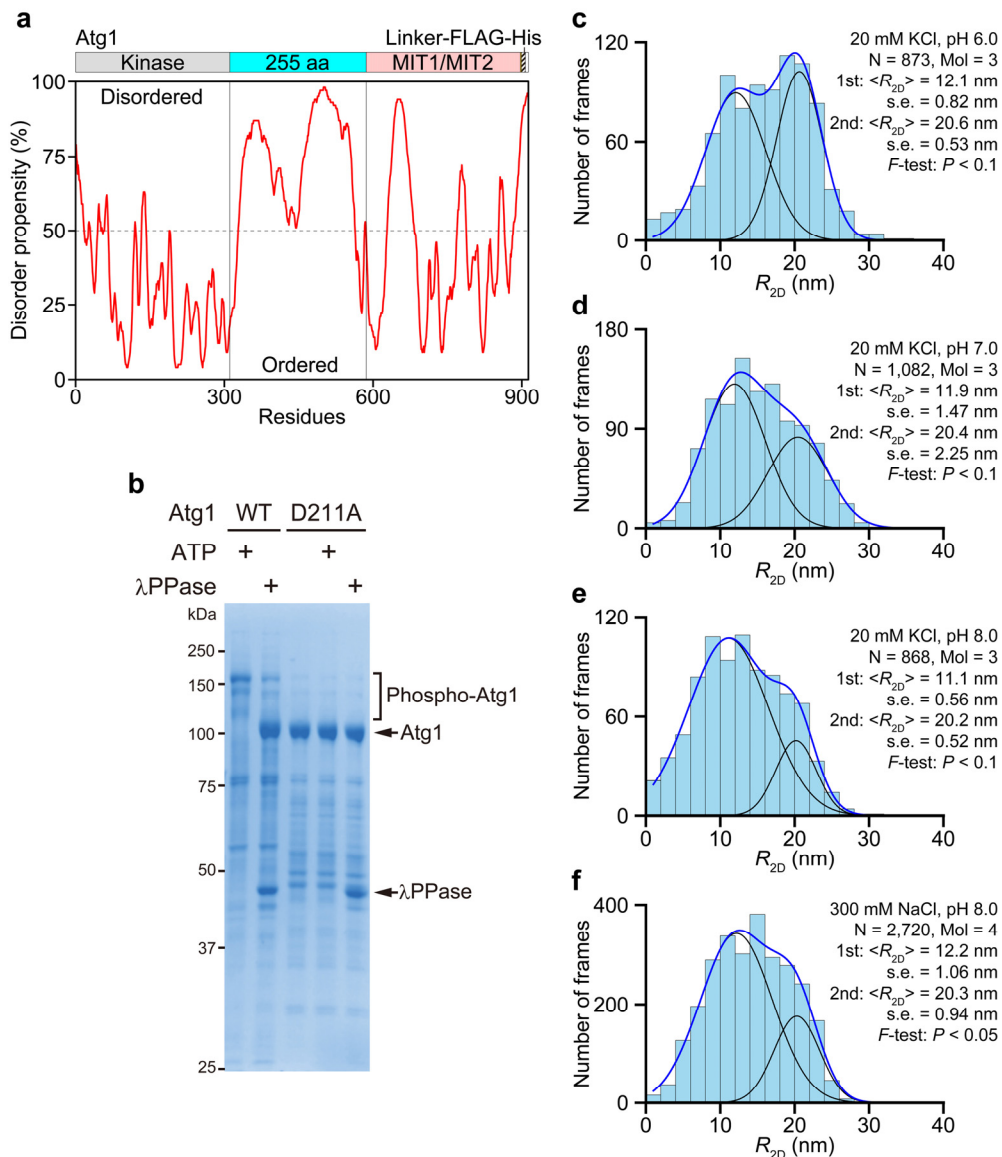
Figure 4 | Structural and dynamic features of N_{TAIL} , PNT and Sic1 revealed by HS-AFM imaging. **a–c**, Domain diagrams of three IDP-GFP fusions. The numbers (top and bottom) are original a.a. sequential numbers and those of the constructs, respectively. **d–f**, HS-AFM images and their schematics of three IDP-GFP fusions. Z-scale, 0.0–3.5 nm. The light-blue arrow-head (**e**, middle) indicates a rarely appearing tiny globule, likely to be α_4 . **g**, Height distribution of GFP in N_{TAIL} -GFP. **h–j**, R_{2D} distributions of N_{TAIL} -GFP (**h**), PNT-GFP (**i**) and Sic1-GFP (**j**). **k–m**, H_2 distributions of N-terminal globules in N_{TAIL} -GFP (**k**), PNT-GFP (**l**) and Sic1-GFP (**m**). **n–p**, Relationship between H_2 and R_{2D} . **q–s**, Schematics showing structural and dynamic features of three IDPs. The top and bottom panels correspond to the more-ordered and less ordered states, respectively. The numbers in red and blue represent the numbers of a.a. contained in the respective small globules and fully disordered IDRs, respectively. The red and blue arrows indicate the kinetic nature of changes in H_2 and R_{2D} , respectively.



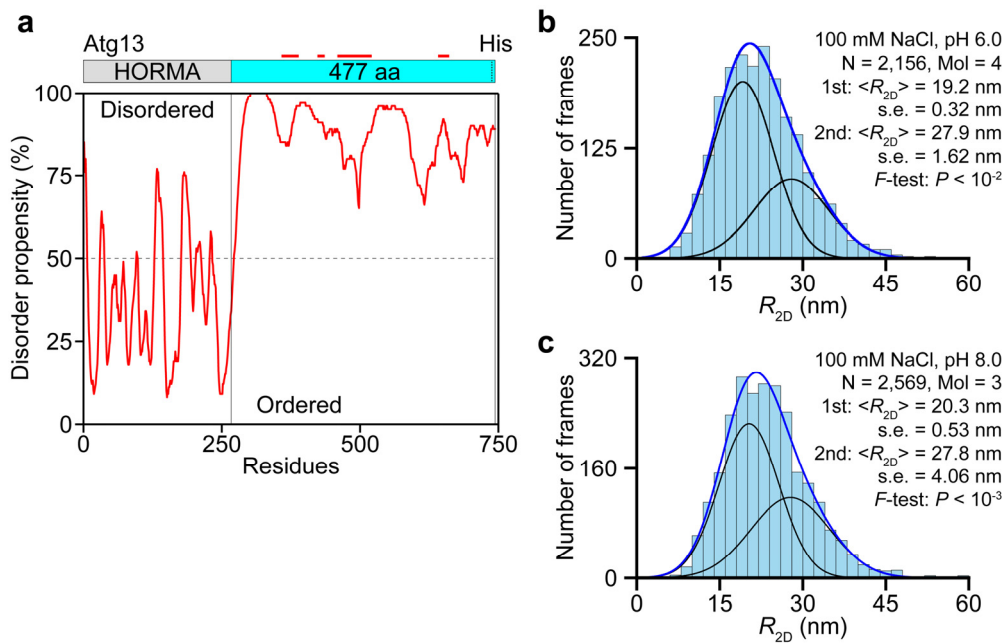
Extended Data Fig. 1 | Molecular features of PQBP-1 (1–214) observed at various imaging rates. **a–f**, H_1 , H_2 and R_{2D} distributions measured from HS-AFM images captured at 6.7 (**a**), 10.0 (**b**), 15.2 (**c**), 20.0 (**d**), 30.3 (**e**) and 50.0 (**f**) fps. The most probable fitting curves are drawn with the solid lines. **g**, $\langle H_1 \rangle$ at various imaging rates. **h**, $\langle H_2 \rangle$ at various imaging rates. **i**, $\langle R_{2D} \rangle$ at various imaging rates. Each plot corresponds to mean values \pm s.e. measured at each frame rate. The horizontal lines indicate the weighted mean values. Details of these analyses are summarized in **Supplementary Table 2**. Note that the intermittent tip-sample contact force becomes larger with increasing imaging rate, whereas the number of contacts *per* frame increases with decreasing imaging rate. Nevertheless, the values of $\langle R_{2D} \rangle$, $\langle H_1 \rangle$ and $\langle H_2 \rangle$ are nearly constant, irrespective of the imaging rate, indicating no significant impact of the tip-sample contact on the structure of this protein.



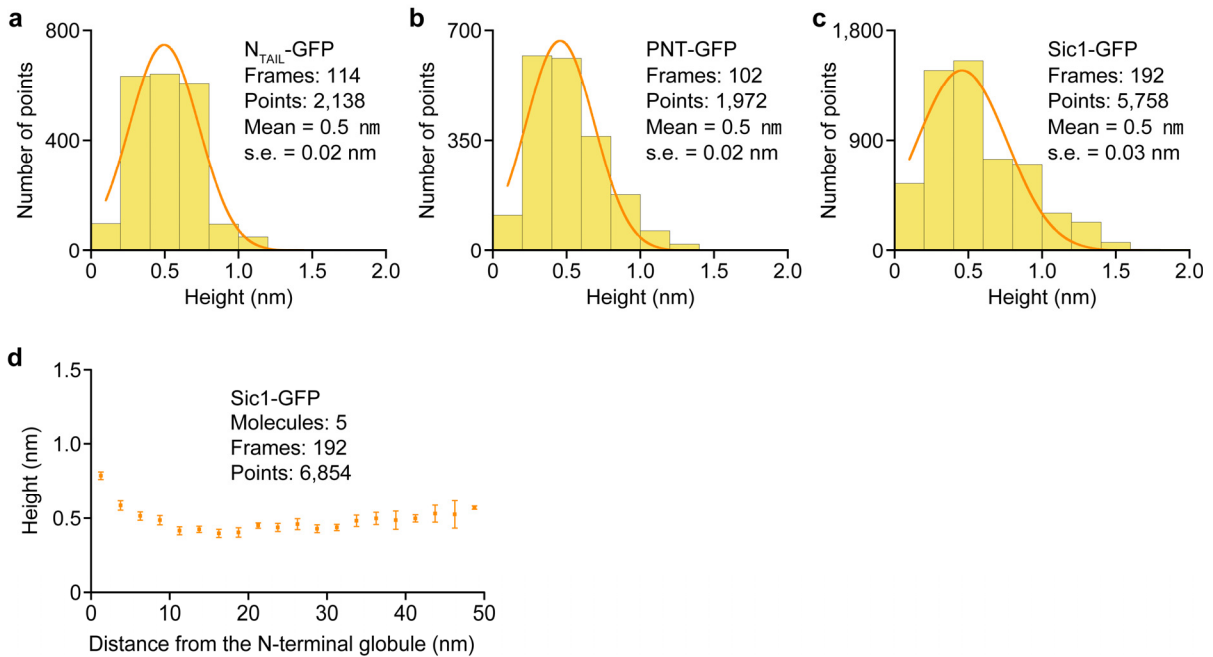
Extended Data Fig. 2 | $I(q)$ curves, Guinier plots, and Kratky plots obtained from SAXS measurements of IDR segments of PQBP-1 (82–134, 82–164, 82–214 and 82–265). a–d, $I(q)$ curves displayed in a q range from 0.018 to 0.500 \AA^{-1} . e–h, Guinier plots displayed in the smaller region of $qR_g < 1.3$. i, Kratky plots normalized by $I(0)$ indicating the fully disordered nature of the four IDRs. A summary of these analyses is presented in **Supplementary Table 3.**



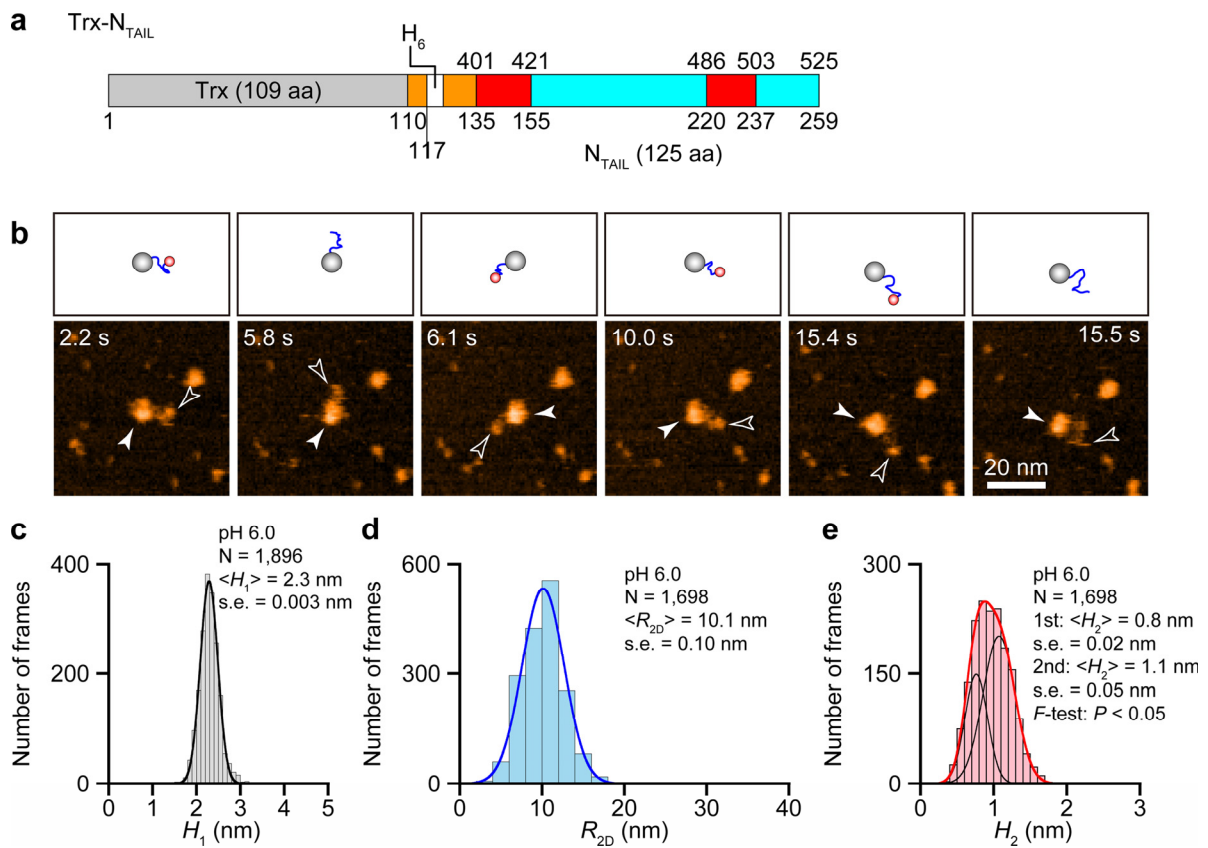
Extended Data Fig. 3 | Characterization of Atg1 (D211A) and R_{2D} distributions of its IDR measured under various solution conditions. **a**, Domain diagram of the Atg1 (D211A) construct (light blue, IDR) and its order/disorder map along its length as predicted by DISPROT (VSL2). **b**, Coomassie Brilliant Blue-stained SDS-PAGE (10%) of WT Atg1 and Atg1 (D211A) showing autophosphorylation of WT Atg1 and no phosphorylation of Atg1 (D211A). The autophosphorylation reaction was performed by incubating 2 μ M Atg1 with 2 mM ATP and 5 mM $MgCl_2$ in 20 mM Tris-HCl, pH 8.0, 150 mM NaCl buffer. The dephosphorylation reaction was performed by incubating 2 μ M Atg1 with 1 μ M lambda protein phosphatase (λ PPase), 2 mM dithiothreitol and 1 mM $MnCl_2$ in the same buffer. These reactions were terminated by the addition of Laemmli SDS sample buffer. **c-f**, R_{2D} distributions of IDR measured under various solution conditions. The most probable fitting curves are shown with the solid blue lines. The black lines represent the Gaussian components in double-Gaussian fitting. Note that the $\langle R_{2D} \rangle$ values at the second peaks (longer states) are nearly identical irrespective of the solution condition, whereas the $\langle R_{2D} \rangle$ values at the first peaks (shorter states) vary depending on the solution condition. A summary of these analyses is presented in **Supplementary Table 4**.



Extended Data Fig. 4 | Order/disorder map along the length of Atg13 and R_{2D} distributions of its IDR measured at two pH values. **a**, Domain diagram of the Atg13 construct used in this study and order/disorder map along its length as predicted by DISPROT (VSL2). The regions indicated by the red bars are 359–389, 424–436 and 641–661 (Atg17-binding regions) and 460–521 (Atg1-binding region). **b,c**, R_{2D} distributions of IDR measured at pH 6.0 (**b**) and pH 8.0 (**c**). The most probable fitting curves are shown with the solid blue lines. The black lines represent the Gaussian components in double-Gaussian fitting. Note that the $\langle R_{2D} \rangle$ values at the second peaks (longer states) are nearly identical irrespective of the solution condition, whereas the $\langle R_{2D} \rangle$ values at the first peaks (shorter states) slightly vary depending on pH. A summary of these analyses is presented in **Supplementary Table 5**.

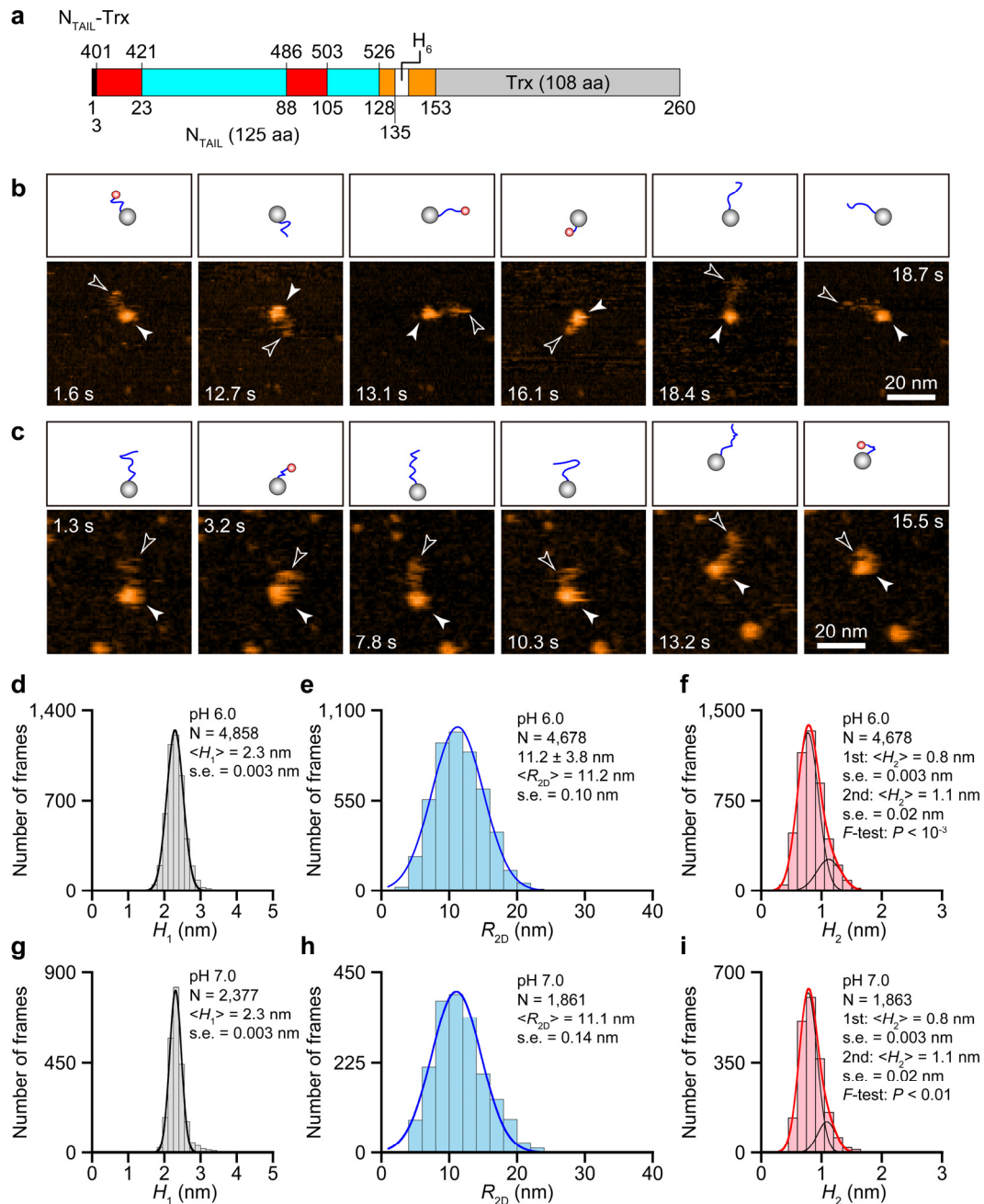


Extended Data Fig. 5 | Height of fully disordered IDRs contained in three IDP-GFP fusions. To make sure that the IDRs under analysis are fully disordered, HS-AFM images showing longer IDRs were chosen. **a**, N_{TAIL} -GFP. **b**, PNT-GFP. **c**, Sic1-GFP. **d**, Height of IDR in Sic1-GFP as a function of its distance from the N-terminus. AFM images of Sic1-GFP molecules showing IDR longer than 25 nm were chosen in this height analysis to ensure that the IDR under analysis was formed upon order-to-disorder transition of the N-terminal small globule. The height of IDR was measured as a function of the distance from the N-terminal globule with a bin width of 2.5 nm. The height values for different frames and molecules measured within the bin width at each lateral distance were averaged and the mean height was plotted together with s.e. The mean height of the N-terminal end (0.8 nm) is slightly smaller than the height of peak 1 (0.9 nm) shown in **Fig. 4m** in the main text. This is due to the relatively large bin width (2.5 nm) of the lateral distance used in this analysis.

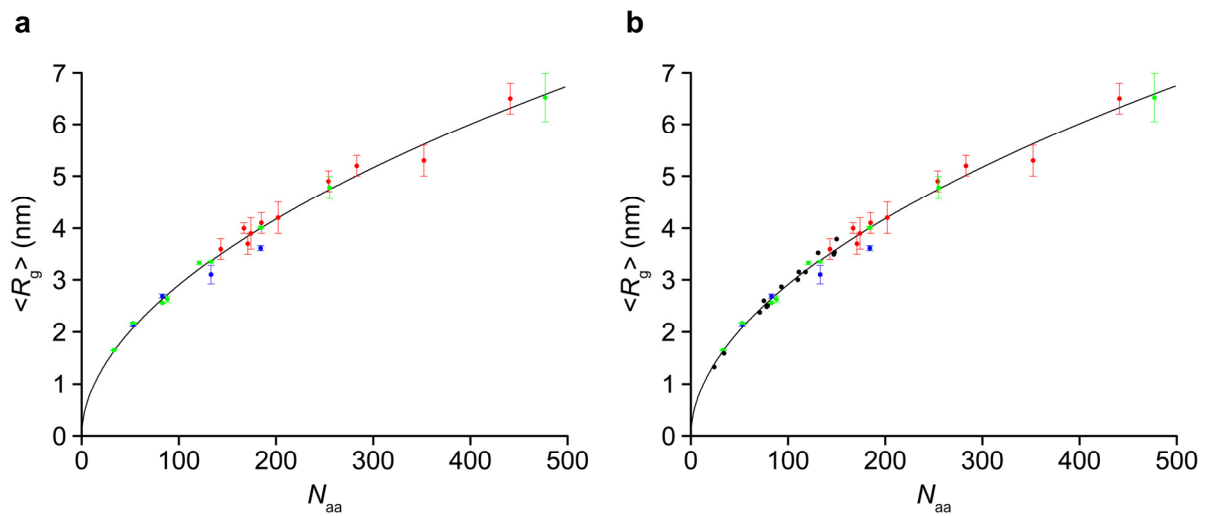


Extended Data Fig. 6 | Structural features of Trx-N_{TAIL} observed by HS-AFM imaging. **a**, Domain diagram of Trx-N_{TAIL} (the a.a. sequence is given in **Supplementary Fig. 1**). Color codes: Gray, Trx; black, Met and Ser; orange, linkers; white, His₆; red, α -More; cyan, IDR. **b**, Successive HS-AFM images of Trx-N_{TAIL} molecules observed at pH 6.0. The molecular features of observed molecules are schematized just above the respective AFM images. The closed and open arrow heads point at the Trx moiety and the tail end, respectively. **c**, Height distribution of the Trx domain. **d**, R_{2D} distribution of the IDR. **e**, Height distribution of the C-terminal globule (Box2). The most probable fitting curves are shown with the thick solid lines. The thin black lines in (e) indicate two Gaussian components in double-Gaussian fitting. A summary of these analyses is presented in **Supplementary Table 7**.

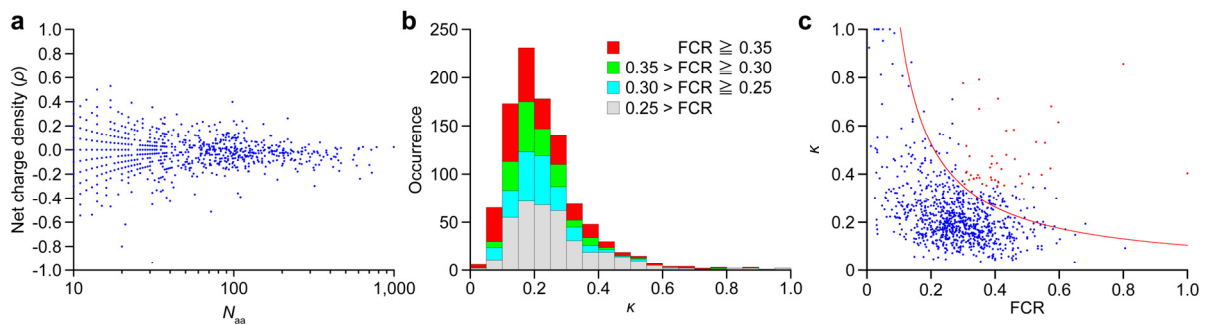
520
521



Extended Data Fig. 7 | Structural features of N_{TAIL} -Trx observed by HS-AFM imaging. **a**, Domain diagram of N_{TAIL} -Trx (the a.a. sequence is given in **Supplementary Fig. 1**). Color code: same as in **Extended Data Fig. 6**. **b,c**, Successive HS-AFM images of N_{TAIL} -Trx molecules observed at pH 6.0 (**b**) and pH 7.0 (**c**). The closed and open arrow heads point at the Trx moiety and the tail end, respectively. **d,g**, Height distributions of the Trx domain measured at pH 6.0 (**d**) and pH 7.0 (**g**). **e,h**, R_{2D} distributions measured at pH 6.0 (**e**) and pH 7.0 (**h**). **f,i**, Height distributions of the N-terminal small globule (Box1) measured at pH 6.0 (**f**) and pH 7.0 (**i**). The most probable fitting curves are shown with thick solid lines (**d-i**). The thin black lines in (**f,i**) are two Gaussian components in double-Gaussian fitting. A summary of these analyses is presented in **Supplementary Table 7**.



Extended Data Fig. 8 | Refinement of expansion effect of mica on the 2D dimensions of IDR and power law for $\langle R_g \rangle$. **a**, $\langle R_g \rangle$ - N_{aa} relationship for 23 data. The 10 data plotted with the red circles are those from the study by Mylonas *et al.* for tau protein constructs⁴⁷, with phosphor-mimic constructs and those significantly affected by the extended repeat domain^{43,49} having been removed here. The constructs herein analyzed are tau ht40, tau K32, tau K16, tau ht23, tau K27, tau K27, tau K44, tau K10, tau K25, and tau K23. The data plotted with the blue circles are those from the present SAXS study for four segments of PQBP-1 IDR (82-265, 82-214, 82-164, and 82-134). The nine data plotted with the green circles are those of $(N_{aa}, \langle R_{2D} \rangle / (2\sqrt{3}u))$ at $u = 1.24$ of the five PQBP-1 constructs, Atg1, Atg13, FACT protein and N_{TAIL} ($\langle R_{2D} \rangle$ data highlighted with orange color in **Supplementary Table 8** are used). The value of u were determined by fitting all 23 data to a power law, $\langle R_g \rangle = \beta_g \times N_{aa}^\nu$, in which the parameter u was contained in the nine data as one of the variables to be determined. The black solid line indicates the best fitting result; $u = 1.24$, $\beta_g = 0.26$ nm, and $\nu = 0.52$. **b**, $\langle R_g \rangle$ - N_{aa} relationship for 37 data. The 37 data points include 14 data found from literature search (black circles; **Supplementary Table 9**) and those 23 data shown in (a). Fitting of the 37 data points to a power law, $\langle R_g \rangle = \beta_g \times N_{aa}^\nu$, yielded $\beta_g = 0.260 \pm 0.021$ nm and $\nu = 0.524 \pm 0.015$ (black line).



Extended Data Fig. 9 | Statistics of charge-associated parameters for many naturally occurring IDRs. **a**, 2D plot of (N_{aa} , ρ) (ρ , charge density) of naturally occurring IDRs whose information is deposited in the Database of Protein Disorder that gathers information of IDRs that have been confirmed to be disordered. The paired values (N_{aa} , ρ) of 1,011 IDRs are plotted in this graph. Half of these data points (50.9%) are within the range of $|\rho| \leq 0.1$. Note that shorter IDRs are enriched in the database, reflecting the fact that short IDPs tend to be more experimentally characterized than longer IDRs. **b**, Histogram of κ for the IDRs contained in the database; IDRs with $N_{aa} \leq 19$ were omitted. Each bar of the histogram is divided into four regions according to the value of fraction of charged residues (FCR). The CIDER software program (opened to public use) was used to calculate the values of κ and FCR (see **Supplementary Note 6**). **c**, Scatter diagram of (FCR, κ) for the IDRs contained in the database; IDRs with $N_{aa} \leq 19$ were omitted. The points shown in red (4.5%) correspond to IDRs that meet the combined condition of $\kappa \geq 0.35$ & $\text{FCR} \geq 0.30$ that is considered to be required for the appearance of a distinct volume compaction effect of oppositely charged residues⁵². It would be plausible that a volume compaction effect could be manifest even for IDRs possessing a FCR value less than (for example) 0.25, when they have a significantly large value of κ . To depict such a possibility, the red line is drawn ($\kappa \times \text{FCR} = 0.35 \times 0.30$). It should be kept in mind however that this is just tentative and awaits future experimental confirmation.

526 **Methods**

527 **Preparation of PQBP-1 constructs.** The DNA encoding full-length PQBP-1 was inserted into a
528 pGEX6P-1 plasmid that was used to transform the *E. coli* BL21 [DE3] strain. Protein expression
529 was induced by the addition of 0.5 mM isopropyl β -D-1-thiogalactopyranoside (IPTG). PQBP-1
530 was expressed as a glutathione S-transferase (GST)-fusion protein. After cultivation, BL21 [DE3]
531 cells were collected by centrifugation. The cells were resuspended in a buffer containing 50 mM
532 sodium phosphate (pH 7.0) and 2 mM dithiothreitol. After cell lysis by sonication and removal of
533 insoluble cell debris by centrifugation, the supernatant was applied to a glutathione sepharose 4B
534 column equilibrated with 50 mM Tris/HCl (pH 7.5), 50 mM NaCl, 1 mM EDTA, and 1 mM
535 dithiothreitol. After washing the column with the same buffer, the GST-fusion protein was eluted
536 from the column by adding 50 mM Tris/HCl (pH 8.5), 50 mM NaCl, and 10 mM reduced
537 glutathione. To obtain PQBP-1, the GST fusion protein was cleaved with a recombinant
538 rhinovirus 3C protease (PreScission protease; GE Healthcare). The cleavage mixture was passed
539 through the glutathione sepharose 4B column to remove GST and 3C protease. PQBP-1 with
540 shorter IDRs and four IDR segments were obtained in the same manner as the full-length PQBP-
541 1. These constructs including WT PQBP-1 were finally purified by reverse phase high-
542 performance liquid chromatography using a 5C8-AR-300 column or a Protein-R column (Nacalai
543 Tesque), followed by dialysis against 20 mM sodium phosphate (pH 7.0). The molecular mass of
544 PQBP-1 and its fragments was confirmed by matrix-assisted laser desorption/ionization time-of-
545 flight mass (MALDI-TOF/MS) spectrometry.

546
547 **Preparation of Atg1 and Atg13.** Expression and purification of Atg1 (D211A) were performed
548 using the baculovirus expression system and tandem chromatography as reported previously²⁸.
549 The DNA encoding C-terminal His₆-tagged full-length Atg13 was inserted into a pET11a
550 plasmid (Novagen) that was used to transform the *E. coli* BL21 [DE3] strain. Protein expression
551 was induced by the addition of 0.1 mM IPTG. After cultivation, BL21 [DE3] cells were collected
552 by centrifugation. The cells were resuspended in a buffer containing 50 mM Tris-HCl (pH 8.0),
553 500 mM NaCl, 10 mM imidazole, 5% (v/v) glycerol, 5mM 2-mercaptoethanol, and Protease
554 Inhibitor Cocktail (Nacalai). After cell lysis by sonication and removal of insoluble cell debris by
555 centrifugation, the supernatant was applied to a Ni-NTA column (Qiagen) equilibrated with 50

556 mM Tris-HCl (pH 8.0), 500 mM NaCl, and 10 mM imidazole. After washing the column with the
557 same buffer, the protein was eluted from the column by adding 50 mM Tris-HCl (pH 8.0), 100
558 mM NaCl, and 200 mM imidazole. Eluents were further purified by gel filtration using a HiLoad
559 26/60 Superdex 200 PG column (GE, Healthcare) and 20 mM Tris-HCl (pH 8.0), 150 mM NaCl
560 as elution buffer. Purified Atg1 (D211A) and Atg13 were concentrated using Centriprep
561 (molecular cutoff of 50,000 Da) (Millipore) and then stored at -80°C .

562
563 **Preparation of GFP-fused proteins.** The constructs encoding the GFP fusion proteins used in
564 this study have been already described⁵³. They all encode for proteins consisting of an N-
565 terminally hexahistidine tagged IDP (N_{TAIL} , PNT or Sic1), followed by a linker of 14 residues
566 containing the tobacco etch virus (TEV) protease cleavage sequence (Glu-Asn-Leu-Tyr-Phe-Gln-
567 Gly-Ser) and the GFP, in this order (**Fig. 4a-c**). The *E. coli* strain Rosetta [DE3] pLysS
568 (Novagen) was used for expression of GFP-fusions. Expression and purification was carried out
569 as already described⁵³ except that immobilized metal affinity chromatography was performed by
570 supplementing both equilibration and elution buffer with 1 M NaCl to get rid of contaminating
571 DNA. Eluents were further purified by gel filtration using a Superdex 200 HR 16/60 column (GE,
572 Healthcare) and 50 mM sodium phosphate pH 7.5, 200 mM NaCl as elution buffer. Proteins were
573 concentrated using Centricon Plus-20 (molecular cutoff of 10,000 Da) (Millipore) and then stored
574 at -20°C .

575
576 **Preparation of Trx-fused N_{TAIL} .** The thioredoxin-6His- N_{TAIL} (Trx-6His- N_{TAIL}) construct was
577 generated as follows. The sequence encoding N_{TAIL} followed by two stop codons was sub-cloned
578 by Gateway technology from an entry clone, whose sequence had been checked by DNA
579 sequencing⁵⁴, into the Gateway expression vector pETG-20A (a gift of Dr. Arie Geerlof, EMBL
580 Heidelberg, Germany) by LR reaction. In this construct, the Trx-6His and N_{TAIL} moieties are
581 separated by a linker (LYKKAGS) encoded by the *Attb1* cloning site borne by the pETG-20A
582 vector. In order to obtain an N_{TAIL} fusion protein only differing for the position of the Trx tag, we
583 designed a construct (referred to as N_{TAIL} -6His-Trx) bearing the same *Attb1*-encoded sequence
584 between the 6His tag and Trx. Since another *Attb1* cloning site is also present in the cloning
585 vector (pDEST14, see below), the *Attb1* sequence added between the 6His tag and Trx was

586 mutated (in italic in the primer sequences given below) in such a way that it could not be
587 recognized by the LR enzyme while still encoding the same linker as *wild-type* attb1.

588 The coding sequence of N_{TAIL} was PCR amplified using the same entry clone bearing the N_{TAIL}
589 coding sequence as above⁵⁴, and primers Attb1-SD-NT

590 (GTACAAAAAAGCAGGCTAATAATTTGTTTAACTTTAAGAAGGAGATATACATATG
591 TCGACTACTgaggacaagatcag)

592 and NT-link

593 (GTCATGGTACCATGATGATGATGATGGTGCCATATGGCCAGAACCAGAACCGTCTAG
594 AAGATTTCTGTCATTG). The coding sequence of Trx was PCR amplified using pETG-20A as

595 template and primers link-TRX

596 (CCATCATCATCATCATGGTACCATGAAGccTGTAtAAgAAgGCgGGtagcAGCGATAAAAT
597 TATTCACC)

598 and TRX-stop-Attb2

599 (ACCACTTTGTACAAGAAAGCTGGGTtattaGGCCAGGTTAGCGTCGAGGAAC).

600 After DpnI digestion, 1µl of each of the first two PCR product were mixed and then used as
601 template in a third PCR amplification with primers attL1a

602 (ACCTGTTTCGTTGCAACAAATTGATGAGCAATGCTTTTTTATAATGCCAAGTTTGTAC
603 AAAAAAGCAGGC)

604 and attL2a

605 (TTTTGACTGATAGTGACCTGTTTCGTTGCAACAAATTGATAAGCAATGCTTTCTTATA
606 ATGCCCACTTTGTACAAGAAAGCTGG)⁵⁵. The third PCR amplification allows to (i) fuse the

607 first two PCR products, (ii) insert a 6His tag (underlined in the above primer sequences) and the
608 Attb1–encoded linker between N_{TAIL} and Trx, (iii) add respectively Attl1a and Attl2a sequences

609 at the 5' and 3' end of the PCR product required for the subsequent cloning step by LR reaction.

610 The product of the third PCR was then inserted into the Gateway vector pDEST14 by LR
611 reaction and checked by DNA sequencing. A detailed description of the two fusion proteins is

612 provided in **Supplementary Fig. 1**.

613 The *E. coli* strain T7pRos⁵⁴ was used for expression of Trx-N_{TAIL} and N_{TAIL}-Trx fusion
614 proteins. Cultures were grown overnight to saturation in LB medium containing 100 µg/mL

615 ampicillin. An aliquot of the overnight culture was diluted 1/25 in LB medium and grown at
616 37 °C. At OD₆₀₀ of 0.7, IPTG was added to a final concentration of 0.5 mM, and the cells were

617 grown at 37 °C for 3 hours. The induced cells were harvested by centrifugation (6,000 g for 20
618 minutes at 4 °C) and resuspended in 30 mL of buffer A (50 mM Tris-HCl, pH 8, 500 mM NaCl,
619 20 mM Imidazole, 1 mM PMSF), supplemented with lysozyme 0.1 mg/mL, DNase I 10 µg/mL,
620 protease inhibitor cocktail (Roche). After a 20-minutes incubation with gentle agitation, the cells
621 were disrupted by sonication (using a 750 W sonicator and 3 cycles of 30 s each at 45% power
622 output). Following the removal of cell debris by centrifugation at 14,000 g for 30 min, the
623 supernatant was applied onto a Ni(II)-loaded 5 mL His-Trap HP column (GE Healthcare)
624 previously equilibrated in buffer A. The affinity resin was washed with 20 column volumes of
625 buffer A containing 1 M NaCl. After this step, the affinity column was connected in tandem to a
626 Superdex 75 16/60 column (GE Healthcare) pre-equilibrated in NaP 10 mM, NaCl 200 mM pH 7
627 buffer. The two connected columns were eluted first using 20 mL of buffer A containing 500 mM
628 imidazole and subsequently using 10 mM phosphate buffer at pH 7, containing 200 mM NaCl.
629 The fractions containing the recombinant protein were collected, lyophilized and stored at -20 °C.
630 For both proteins, mass spectrometry analysis yielded a value that fits perfectly with the expected
631 molecular mass for a form in which the initial methionine has been cleaved off.

632
633 **SAXS analysis.** SAXS measurements were performed at 23°C with a BioSAXS-1000 system
634 (Rigaku) mounted on a MicroMx007HF X-ray generator (Rigaku). A PILATUS100K detector
635 (DECTRIS) at a distance of 462 mm from the sample, was used to measure scattering intensities.
636 The IDR segments of PQBP-1 (82-134, 82-164, 82-214 and 82-265) in 10 mM phosphate
637 buffer (pH6.0) were used for SAXS measurements. Circular averaging of the scattering
638 intensities was carried out to obtain one-dimensional scattering data $I(q)$ as a function of q ($q =$
639 $4\pi \sin\theta/\lambda$, where 2θ is the scattering angle and λ is the X-ray wavelength 1.5418 Å) by using the
640 program SAXSlab (Rigaku). The $I(q)$ data were processed by using the software applications
641 embedded in the ATSAS package⁵⁶. The radius of gyration R_g and forward scattering intensity
642 $I(0)$ were estimated from the Guinier plot of $I(q)$ in the smaller angle region of $qR_g < 1.3$. The
643 molar mass of the IDR segments were estimated by comparing $I(0)/c$ (where c is the protein
644 concentration) of the IDR segments to that of ovalbumin, or estimated from Q_R ⁵⁷. To correct
645 interparticle interference, $I(q)$ data were collected at three different protein concentrations (10, 8,
646 and 6 mg/ml for 82-134 and 82-164. 5, 3, and 0.3 mg/ml for 82-214. 14, 10, and 8 mg/ml for
647 82-265). Because the intensity profile of 82-134, 82-164 and 82-265 did not indicate a

648 concentration effect, the correction for interparticle interference was not applied. 82–214
649 fragment exhibited weak self-association at 5 mg/ml and 3 mg/ml. Therefore, a diluted sample
650 (0.3 mg/ml) was used for structural analysis. SAXS data are summarized in **Extended Data Fig.**
651 **2** and **Supplementary Table 3**.

652
653 **HS-AFM observation.** The procedure for HS-AFM observation of protein dynamics at the
654 single-molecule level has already been described⁵⁸. In brief, a glass sample stage (diameter, ~2
655 mm; height, ~2 mm) with a thin mica disc (1 mm in diameter and 0.05 mm thick) glued to the top
656 by epoxy was attached onto the top of the Z-scanner by a drop of nail polish. A freshly cleaved
657 mica surface was prepared by removing the top layers of mica using Scotch tape. Then a drop (~2
658 μ l) of the diluted sample (~3 nM) was deposited onto the mica surface. After an incubation of
659 about 3 minutes, the mica surface was rinsed with 20 μ l of an observation buffer shown below for
660 each sample to remove floating samples. The sample stage was then immersed in a liquid cell
661 containing ~60 μ l of the same observation buffer. HS-AFM observation was performed in the
662 tapping mode using a laboratory built apparatus^{14,15}. The short cantilevers used are custom-made
663 by Olympus (Tokyo, Japan); resonant frequency, ~1 MHz in water; quality factor, ~2 in water;
664 spring constant, 0.1–0.15 N/m. The cantilever's free oscillation amplitude A_0 and set point
665 amplitude A_s were set at 1–2 nm and $\sim 0.9 \times A_0$, respectively, so that the loss of cantilever's
666 oscillation energy per tap was adjusted to be 1–3 $k_B T$ on average. The imaging rate, scan size and
667 the pixel size for each sample are described in the main text and Supplementary information. The
668 observation buffers used for the respective IDPs are as follows:

PQBP-1	10 mM Sodium phosphate buffer, pH 6.0
Atg1	20 mM KCl, and 20 mM Tris-HCl, pH 6.0
	20 mM KCl, and 20 mM Tris-HCl, pH 7.0
	20 mM KCl, and 20 mM Tris-HCl, pH 8.0
	50 mM NaCl, and 20 mM Tris-HCl, pH8.0
	300 mM NaCl, and 20 mM Tris-HCl, pH8.0
Atg13	100mM NaCl and 20 mM Tris-HCl, pH 6.0
	100mM NaCl and 20 mM Tris-HCl, pH 7.0
	100mM NaCl and 20 mM Tris-HCl, pH 8.0

FACT-10SA	50 mM KCl, 10 mM MgCl ₂ , 20 mM Tris-HCl, pH 7.5 and 0.5% glycerol (vol/vol)
N _{TAIL} -GFP	10 mM Sodium phosphate buffer, pH 6.0
N _{TAIL} -Trx	10 mM Sodium phosphate buffer, pH 6.0 10 mM Sodium phosphate buffer, pH 7.0
Trx- N _{TAIL}	10 mM Sodium phosphate buffer, pH 6.0
PNT-GFP	10 mM Sodium phosphate buffer, pH 6.0
Sic1-GFP	10 mM Sodium phosphate buffer, pH 6.0

669

670 **Analysis of AFM images.** To measure topographical parameters (R_{2D} , H_1 and H_2), we used a
671 pixel-search software program that we had made for a previous HS-AFM study⁵⁹. This program
672 is opened to the public at the following web site:

673 <https://elifesciences.org/content/4/e04806/article-data#fig-data-supplementary-material>

674 First, AFM images are briefly pretreated (mostly flattened for scan line non-horizontality) by our
675 AFM-specific data acquisition software. From an AFM image, the operator roughly finds an end
676 region of IDR and then clicks the mouse pointer at a molecule-free position on the surface that
677 appears very close to the end region. Then, the pixel search program automatically finds a pixel
678 position (X , Y) having the largest height Z , by searching over $n \times n$ pixels around the operator-
679 specified pixel position (the value of n is appropriately chosen; typically $n = 5$). The height H
680 (H_1 or H_2) is obtained by subtracting the average height of the substrate surface from the Z value.
681 The same procedure is repeated at the other end of the IDR. From the obtained two sets of (X , Y)
682 coordinates, the direct distance D between the two pixels is calculated, which is followed by a
683 calculation of R_{2D} value as $R_{2D} = D - H_1/2 - H_2/2$. The autocorrelation functions $G(\tau)$ of time
684 series data $x(n\Delta t)$ of R_{2D} and H_2 were calculated as

$$685 \quad G(\tau) \equiv \frac{\sum_{n=1}^{N-h} [x(n\Delta t) - \hat{\mu}] [x((n+h)\Delta t) - \hat{\mu}]}{\sum_{n=1}^N [x(n\Delta t) - \hat{\mu}]^2},$$

686 where $\tau \equiv h\Delta t$ and $\hat{\mu}$ is the mean value of $x(n\Delta t)$ ($n = 1, 2, 3, \dots, N$).

687

688 **References for Methods**

- 689 53. Sambti, I., Gatti–Lafranconi, P., Longhi, S. & Lotti, M. How disorder influences order and
690 vice versa – mutual effects in fusion proteins containing an intrinsically disordered and a
691 globular protein. *FEBS J.* **277**, 4438–4451 (2010).
- 692 54. Gruet, A., Longhi, S. & Bignon, C. One-step generation of error-prone PCR libraries using
693 Gateway® technology. *Microb Cell Fact.* **11**, 14 (15 pp) (2012).
- 694 55. Gruet, A. et al. Fuzzy regions in an intrinsically disordered protein impair protein-protein
695 interactions. *FEBS J.* **283**, 576–594 (2016).
- 696 56. Petoukhov, M. V. et al. New developments in the ATSAS program package for small-angle
697 scattering data analysis. *J. Appl. Cryst.* **45**, 342–350 (2012).
- 698 57. Rambo, R. P. & John A. Tainer, J. A. Accurate assessment of mass, models and resolution by
699 small-angle scattering. *Nature* **496**, 477–481 (2013).
- 700 58. Uchihashi, T., Kodera, N. & Ando, T. Guide to video recording of structure dynamics and
701 dynamic processes of proteins by high-speed atomic force microscopy. *Nat. Protoc.* **7**, 1193–
702 1206 (2012).
- 703 59. Ngo, K. X., Kodera, N., Katayama, E., Ando, T. & Uyeda, T. Q. P. Cofilin-induced
704 unidirectional cooperative conformational changes in actin filaments revealed by high-speed
705 AFM. *e-Life* **4**, e04806 (2015).
- 706